# Impacts of synoptic circulation types on nocturnal ozone increase in the North China Plain: Meteorological drivers and physical ~~formation~~ mechanisms

Huanpeng Wang[1], Liya Fan[1,2,3,4*], Xuejiao Deng[5], Haomin Huang[1,2,3,4], Daiqi Ye[1,2,3,4]

[1]School of Environment and Energy, South China University of Technology, Guangzhou, 510006, China
[2]National Engineering Laboratory for Volatile Organic Compounds Pollution Control Technology and Equipment, Guangzhou, 510006, China
[3]Guangdong Provincial Key Laboratory of Atmospheric Environment and Pollution Control, Guangzhou, 510006, China
[4]Guangdong Provincial Engineering and Technology Research Centre for Environmental Risk Prevention and Emergency Disposal, Guangzhou, 510006, China
[5]Key Laboratory of Regional Numerical Weather Prediction, Guangzhou Institute of Tropical and Marine Meteorology, China Meteorological Administration, Guangzhou, 510680, China

*Correspondence to*: Liya Fan (fanly@scut.edu.cn)

**Abstract.** ~~Nocturnal ozone increase (NOI) has become common worldwide, raising the risk of ozone pollution. Weather types serve as one of the critical drivers of NOI, but how they influence NOI remains poorly understood. Using ground observation and reanalysis datasets, this study identified the relationship between weather types and NOI days in a representative city on the North China Plain, and investigated the meteorological characteristics and formation mechanisms of NOI days under different weather types. During 2021-2023, 392-470 NOI days were observed, with the occurrence predominantly concentrated between 00:00 and 06:00 local time (71.35%). Based on the Lamb-Jenkinson method, NOI days were classified into four primary weather types: A-type (57.36%), C-type (11.17%), S-type (20.81%) and WNE-type (10.66%). A-type was dominated by high-pressure anticyclones with mild weather condition, whereas C-type was controlled by low-pressure systems and influenced by moist airflows. S-type was located in the transition zone between high and low pressure, influenced by southern geostrophic winds, and WNE-type was characterized by high-pressure systems with W-N-E geostrophic flows. Notably, under all four weather types, the formation of NOI days was attributed to the synergy of regional and vertical transport. Specifically, under S-type and WNE-type, regional transport was influenced by geostrophic winds, while vertical transport was associated with high-pressure subsidence (A-type and WNE-type), cold-pool subsidence (C-type), and shallow convection (S-type). This study elucidates the diverse dynamical pathways of weather-driven NOI, and provides mechanistic insights for improving ozone forecasting and mitigation strategies in urban environments.~~Nocturnal ozone ($O_3$) increase (NOI) has become common worldwide, raising the risk of $O_3$ pollution. While weather types serve as critical drivers of NOI, their specific dynamic influences remain poorly understood. Using ground observations and reanalysis datasets, this study identified the relationship between weather types and NOI days in a representative city in the North China Plain, and revealed the meteorological characteristics and physical mechanisms driving these events. During 2021-2023, 370-444 NOI days were observed, with the occurrence predominantly concentrated between 00:00 and 06:00 local time (69.53%). After screening, a total of 171

representative NOI days were finally identified to characterize the overall occurrence of local NOI events. Based on the Lamb-Jenkinson method, the representative NOI days were classified into four primary weather types: A-type (57.89%), S-type (19.88%), WNE-type (14.04%), and C-type (8.19%). A-type was dominated by high-pressure anticyclones with calm conditions, whereas C-type was controlled by low-pressure systems and influenced by moist airflows. S-type was located in the transition zone between high and low pressure, influenced by southern geostrophic winds, and WNE-type was characterized by high-pressure systems with W-N-E geostrophic flows. Distinct mechanical triggers for NOI were further resolved for different types: A-type is dominated by high-pressure subsidence; C-type is driven by cold-pool downdrafts and convective motions; whereas both S-type and WNE-type are primarily controlled by synoptically-driven intense wind shear. This study elucidates the diverse dynamical pathways of weather-driven NOI, providing mechanistic insights for improving $O_3$ forecasting and mitigation strategies in urban environments.

## 1 Introduction

Surface ozone ($O_3$), a typical secondary pollutant, poses significant risks to human health due to its strong oxidative properties (Paoletti, 2009; Monks et al., 2009). Excessive $O_3$ can lead to increased incidence and mortality rates of asthma, cardiovascular and respiratory diseases (Liu et al., 2023; Cheng et al., 2022; Gilardi et al., 2023; Zhao et al., 2022). Formed primarily through photochemical reactions of volatile organic compounds (VOCs) and nitrogen oxides ($NO_x$) under sunlight (Li et al., 2022b; Li et al., 2022a; Wang et al., 2023a), $O_3$ typically peaks during the daytime and declines at night due to deposition and $NO_x$ titration (Li et al., 2022b; Shen et al., 2024; He et al., 2021; Zhu et al., 2020). In China, despite successful reductions in particulate matter (PM) since the 2013 Air Pollution Prevention and Control Action Plan, $O_3$ pollution has intensified, particularly in the North China Plain (NCP) (Shen et al., 2024; Xu et al., 2021; Dong et al., 2020; Song et al., 2022). Meanwhile, recent observations in the NCP have revealed an unexpected phenomenon of nocturnal $O_3$ increase (NOI) (He et al., 2021; Zhu et al., 2020). The occurrence of NOI not only increases nighttime $O_3$ levels but also poses a potential risk of $O_3$ pollution on the following day. Previous studies have demonstrated NOI's promoting effect on $O_3$ pollution (Wang et al., 2025; He et al., 2022; Wang et al., 2023d; Zhu et al., 2020), but the underlying mechanisms and contributing drivers of NOI are not yet fully understood.

NOI events, characterized by unexpected rises in nighttime $O_3$ concentrations (at least 10 μg $m^{-3}$ per hour (Zhu et al., 2020)), challenge the conventional understanding of $O_3$ (Wang et al., 2023b; Xue et al., 2023; Chen et al., 2024b). Previously, nocturnal $O_3$ was often overlooked owing to its low concentrations. Although a quantitative threshold of a 10 μg $m^{-3}$ hourly increase may appear modest during a clean night, the scientific and environmental significance of NOI episodes extends far beyond simple numerical detection. First, NOI events can occasionally result in a rapid surge in nighttime $O_3$ levels surpassing 160 μg $m^{-3}$~~However, the occurrence of NOI events can result in a rapid surge in nighttime $O_3$ levels, with hourly concentrations even surpassing 160 μg $m^{-3}$~~ (Wang et al., 2023d; Zhu et al., 2024), directly posing nocturnal threats to human health and plant stomatal uptake~~. High concentrations of nocturnal $O_3$ also have a significant impact on human health and plant growth~~

(Chowdhury et al., 2022; Hoshika et al., 2019). More critically, even when absolute concentrations remain moderate, the horizontal or vertical transport of $O_3$-rich air that typically triggers NOI significantly elevates the surface $O_3$ baseline for the following morning. This higher initial baseline accelerates daytime accumulation, effectively exacerbating subsequent daytime photochemical smog (Wang et al., 2025). Furthermore, unexpected nighttime $O_3$ increments fundamentally alter the nocturnal atmospheric oxidative capacity (AOC). The enhanced $O_3$ facilitates dark reactions with nitrogen dioxide ($NO_2$) to generate nitrate radicals ($NO_3$) and dinitrogen pentoxide ($N_2O_5$), critical precursors for particulate nitrate and secondary organic aerosols (SOA), thereby linking NOI directly to regional fine particulate matter ($PM_{2.5}$) pollution (Wang et al., 2023b). NOI events, usually driven by horizontal and vertical transport processes, are linked to meteorological phenomena ~~activities~~ such as sea-land winds (Nair et al., 2002), valley winds (Sánchez et al., 2005; Xue et al., 2023), low-level jets and convective storms (Zhu et al., 2020; Wu et al., 2023). While daytime $O_3$ pollution is well-documented, NOI remains poorly understood, necessitating the research into its meteorological drivers and physical ~~formation~~ mechanisms.

Apart from emissions of $O_3$ precursors, meteorological conditions play a crucial role in $O_3$ formation (Dong et al., 2020). Weather conditions of high temperature, low humidity, and strong solar radiation are conducive to the photochemical generation of $O_3$ (Liang et al., 2022; Chen et al., 2024b). The environment of low wind speed and high-pressure often leads to stagnant weather conditions, resulting in localized $O_3$ accumulation (Liu et al., 2025). These weather conditions are largely determined by local synoptic circulation types (Xu et al., 2021; Song et al., 2022; Chen et al., 2024b; Li et al., 2023). For example, Shen et al. (2024) found that persistent $O_3$ pollution events over Wuxi from 2014 to 2021 were primarily associated with subtropical high-pressure and weak pressure systems, characterized by dry and hot local weather conditions. Ji et al. (2023) reported that high $O_3$ concentrations in southeastern coastal areas of China from 2015 to 2020 were mainly linked to high-pressure anticyclonic activity, which frequently occurs in spring. You et al. (2024) observed that $O_3$ pollution in the Pearl River Delta region during autumn from 2015 to 2021 was often influenced by the Siberian high-pressure system, with significant cross-regional transport from the northeast. ~~These studies highlight the role of weather types in $O_3$ pollution, yet the specific meteorological drivers of NOI remain underexplored, particularly in rapidly urbanizing regions like the NCP.~~However, while the relationship between weather types and daytime photochemical $O_3$ is well-established, their specific dynamic roles in driving nighttime NOI remain underexplored, particularly in rapidly urbanizing regions like the NCP.

Located in the southern NCP, Xinxiang is bordered by the Taihang Mountains to the north and the Yellow River to the south (Fig. S1). As a densely populated urban center (with a population exceeding 6 million and a high population density of over 700 persons $km^{-2}$), Xinxiang features a typical temperate continental monsoon climate, characterized by hot, humid summers and cold, dry winters. Furthermore, serving as a major industrial and transportation hub in Henan Province, the city experiences intense anthropogenic emissions. The primary precursors for $O_3$ (i.e., $NO_x$ and VOCs) predominantly originate from heavy industrial facilities (e.g., chemical and manufacturing plants), intense vehicular exhaust along major transportation arteries, and solvent usage. This unique topography, combined with these high baseline emissions and specific climatological conditions, makes Xinxiang a critical case study for understanding NOI. ~~Located in the southern NCP, Xinxiang is an industrial and transportation hub bordered by the Taihang Mountain to the north and the Yellow River to the south (Fig. S1). This unique~~

topography, combined with high emissions, makes Xinxiang a critical case study for understanding NOI. This study aims to bridge the gap between synoptic-scale drivers and local NOI occurrences. By integrating three-year (2021-2023) high-frequency observations with the Lamb-Jenkinson method, we (1) investigate the temporal variability characteristics of NOI, (2) identify the dominant synoptic circulation types conducive to NOI, and (3) unravel the distinct physical mechanisms that govern NOI under different weather types. These insights not only enhance our understanding of the nocturnal $O_3$ budget but also provide a scientific basis for improving $O_3$ forecasting and mitigation strategies in urban environments.

## 2 Data and methods

### 2.1 Data sources

Hourly ground observation data including $O_3$ concentration, temperature, relative humidity, wind speed, wind direction and precipitation were obtained from four national monitoring stations in Xinxiang (named Development Zone (KF), Environmental Protection East Hospital (DY), Environmental Protection West Court (XY) and Municipal Party School (DX), respectively). It is important to note that all four stations are officially classified as urban evaluation sites located within the urban areas of Xinxiang. In this study, these four stations were deliberately selected due to their strong spatial representativeness over the urban core and their high data completeness. Because these stations share a consistent urban typology, they experience highly comparable baseline chemical environments (e.g., similar baseline nitrogen monoxide (NO) titration sinks and anthropogenic precursor availability). This spatial consistency is a crucial methodological design: it effectively minimizes random micro-scale chemical biases and isolated emission noise. By strictly controlling for these localized chemical heterogeneities, we ensure that the concurrent NOI events captured by this network genuinely reflect the overarching regional synoptic forcing and its subsequent, synchronized mechanical disruption of the local boundary layer, rather than random chemical artifacts. Detailed station information is provided in Fig. S1.~~The detailed information is shown in Fig. S1.~~ Sea level pressure (SLP) data and 17-layer vertical profiles (500-1000 hPa) of vorticity, wind speed (WS), wind direction, temperature (T), relative humidity (RH) and $O_3$ concentration were acquired from the Modern-Era Retrospective Analysis for Research and Applications dataset (MERRA-2, Version 2, with a spatial resolution of 0.5° × 0.625° and temporal resolutions of 1 hour for surface data and 3 hours for 3D vertical profiles) (https://disc.gsfc.nasa.gov/). This dataset was constructed by NASA Global Modeling and Assimilation Office (GMAO) using the Goddard Earth Observing System (GEOS) assimilation model, and has been widely applied in weather typing studies worldwide (Zhang et al., 2022; Gelaro et al., 2017; Molod et al., 2015; Li et al., 2020b). Additionally, specific humidity (850hpa), planetary boundary layer height (PBLH), friction velocity ($U^*$), and convective available potential energy (CAPE) were derived from the ERA5 reanalysis dataset (https://www.ecmwf.int/en/forecasts/dataset/ecmwf-reanalysis-v5) (with a spatial resolution of 0.25° × 0.25° and an hourly temporal resolution) provided by the European Centre for Medium-Range Weather Forecasts (ECMWF), which offers superior boundary layer parameters (Hersbach et al., 2020; Bell et al., 2021). Notably, the 850 hPa pressure level (approximately 1500 m above ground level) was specifically selected for the spatial wind field analysis. Because this altitude generally resides just

above the planetary boundary layer, the airflow is largely free from localized surface friction and complex topographic disturbances. Consequently, it serves as the most representative level for identifying mesoscale horizontal advection, low-level jets, and regional synoptic transport pathways that drive $O_3$ redistribution.

### 2.2 Definition of NOI events and NOI days

NOI event is defined as an hourly $O_3$ concentration increment exceeding 10 μg $m^{-3}$ during nighttime (20:00-06:00 local time, LT; UTC+8, Beijing Time) (He et al., 2021; Zhu et al., 2020). This absolute increment threshold is widely adopted in current literature (Zhu et al., 2024; Zhu et al., 2020; He et al., 2022; Wang et al., 2025) because it acts as an indicator for detecting the abrupt physical intrusion of $O_3$-rich air masses into local surface. While the absolute baseline concentrations and temporal trajectories of $O_3$ are crucial for evaluating human health exposure and long-term air quality attainment, the primary objective of this study is to isolate the underlying synoptic and meteorological transport mechanisms. Regardless of the initial surface baseline, a sudden hourly surge of >10 μg $m^{-3}$ effectively and consistently flags that sudden dynamic transport processes (whether via robust horizontal advection, massive vertical subsidence, or other regional intrusions) have completely overpowered the steady local nocturnal depletion (e.g., NO titration and dry deposition). Therefore, this increment-based metric provides the most robust and objective foundation for our dynamical and meteorological analysis.

Considering the seasonal variation in local sunrise time, we excluded NOI events occurring after 05:00 LT from April to September, when the sunrise occurs relatively early. Since nighttime generally lasts from 20:00 to 06:00 LT the next day, it constitutes a continuous process. Therefore, a day is classified as an NOI day if such events occur from 20:00 to 06:00 LT the next day (excluding April to September, for which the window is 20:00 to 05:00 LT). By strictly confining the concept of NOI days to this continuous nocturnal window, we ensure that our dynamic analysis remains completely isolated from daytime photochemical interference. To further investigate the temporal occurrence characteristics within this continuous night, we subsequently categorized these NOI days into three descriptive types. Rather than using arbitrary mathematical intervals, the specific timeframes for these types were chosen to perfectly align with the distinct physical evolution phases of the nocturnal boundary layer: (1) Early-night NOI (EN): The event occurs only between 20:00 and 23:00 LT, corresponding to the transitional boundary layer phase; (2) Late-night NOI (LN): The event occurs only between 00:00 and 06:00 LT, corresponding to the highly stable surface inversion phase; (3) Whole-night NOI (WN): The event occurs across both periods, persisting continuously through the night.~~A day is classified as an NOI day if such events occur either during 00:00-06:00 or 20:00-23:00 LT. Based on the occurrence time of NOI, NOI days are categorized into three types: Type A, NOI occurs only between 00:00 and 06:00 LT; Type B, NOI occurs only between 20:00 and 23:00 LT; Type C, NOI occurs both 00:00-06:00 and 20:00-23:00 LT.~~

### 2.3 Lamb-Jenkinson synoptic circulation classification approach

The Lamb-Jenkinson synoptic circulation classification approach serves as a precise and efficient meteorological classification method, which has been widely used in many studies (Zhu et al., 2007; Duan et al., 2020; Wu et al., 2020; Wang et al., 2023e).

In this study, 16 grid points were selected around Xinxiang in accordance with Lamb-Jenkinson approach. The grid points cover the region from 25°N to 45°N and 100°E to 130°E, with a grid spacing of 5° in latitude and 10° in longitude (Fig. S2). To accurately capture the synoptic background driving NOI events and to eliminate daytime boundary layer convective perturbations, the classification was performed using strictly nocturnal SLP fields rather than daily averages. Furthermore, a seasonally-adjusted nocturnal window was applied based on local sunrise times, consistent with the nocturnal time window adopted for NOI. Based on SLP data from the selected grid points, 6 circulation indices were calculated (Zhou et al., 2023; You et al., 2024; Liu et al., 2019). The corresponding calculation formulas and circulation indices are introduced as follows:

$$u=0.5(P12+P13-P4-P5) \quad (1)$$

$$v=\frac{1}{\cos\alpha}\times\frac{1}{4}(P5+2P9+P13-P4+2P8-P12) \quad (2)$$

$$V=\sqrt{u^2+v^2} \quad (3)$$

$$\xi_u=\frac{\sin\alpha}{\sin\alpha_1}\times\frac{1}{2}(P15+P16-P8-P9)-\frac{\sin\alpha}{\sin\alpha_2}\times\frac{1}{2}(P8+P9-P1-P2) \quad (4)$$

$$\xi_v=\frac{1}{2\cos^2\alpha}\times\frac{1}{4}(P6+2P10+P14-P5-2P9-P13-P4-2P8-P12+P3+2P7+P11) \quad (5)$$

$$\xi=\xi_u+\xi_v \quad (6)$$

$$b_1=\arctan(u/v) \quad (7)$$

$$b_2=\arctan(u/v)+180° \quad (8)$$

where u and v represent the zonal and meridional components of the geostrophic wind, respectively. V is the geostrophic wind. $\xi_u$ and $\xi_v$ are the meridional gradient of u and the zonal gradient of v, respectively. $\xi$ is the geostrophic vorticity. P1-P16 are SLP at 16 grid points. $\alpha$, $\alpha_1$, and $\alpha_2$ represent the latitude of the grid points of P8, P12, and P4, respectively. When $v < 0$, $b_1$ is the geostrophic wind direction. When $v > 0$, $b_2$ is the geostrophic wind direction.

According to each circulation index and geostrophic wind direction, 27 weather types were classified (Table 1) (You et al., 2024; Liu et al., 2019).

**Table 1. Lamb-Jenkinson synoptic circulation classification.**

| $\|\xi\| \le V$ (directional types) | $V < \|\xi\| < 2V$ (hybrid types) | $\|\xi\| \ge 2V$ (vorticity types) | other |
|---|---|---|---|
| N (north) | AN (anticyclone + north) | A (anticyclone) | UD (undefined) |
| E (east) | AE (anticyclone + east) | C (cyclone) | |
| S (south) | AS (anticyclone + south) | | |
| W (west) | AW (anticyclone + west) | | |
| NE (northeast) | ANE (anticyclone + northeast) | | |
| SE (southeast) | ASE (anticyclone + southeast) | | |
| SW (southwest) | ASW (anticyclone + southwest) | | |
| NW (northwest) | ANW (anticyclone + northwest) | | |
| | CN (cyclone + north) | | |

| |
|---|
| CE (cyclone + east) |
| CS (cyclone + south) |
| CW (cyclone + west) |
| CNE (cyclone + northeast) |
| CSE (cyclone + southeast) |
| CSW (cyclone + southwest) |
| CNW (cyclone + northwest) |

### 2.4 HYSPLIT and CWT

The hybrid single particle lagrangian integrated trajectory (HYSPLIT) is a common model for investigating meteorological transmission channels (Chen et al., 2024a; Cheng et al., 2024; Shi et al., 2024; Stein et al., 2015). It can efficiently and accurately determine the transport trajectories of different pollutants, classify and aggregate the backward trajectories during the study period through the Euler clustering method, and output air mass trajectories with different proportions. In this study, the HYSPLIT model (run via the TrajStat plugin / MeteoInfo) was used to identify backward trajectories for Xinxiang during the period from 2021 to 2023. The model inputs hourly meteorological data from the Global Data Assimilation System with a spatial resolution of 1° × 1° (ftp://arlftp.arlhq.noaa.gov/pub/archives/gdas1). Taking the starting point (central location of Xinxiang: 35.30°N, 113.88°E) as a reference, 48-hour backward trajectories terminating at 100 m above ground level were calculated at 1-hour intervals for all identified representative NOI days. Using these air mass trajectories, we mapped $O_3$ concentrations to specific geographic grids to apply Concentration-Weighted Trajectory (CWT) analysis. Briefly, the CWT approach calculates the weighted average concentration of air mass trajectories passing through each 1° × 1° grid cell, thereby quantitatively identifying the relative contributions of potential upwind source regions to local $O_3$ spikes (Shi et al., 2024; Wang et al., 2024). To mitigate statistical uncertainties from grid cells with sparse trajectory endpoints, an empirical weighting function $W_{ij}$ was incorporated. The complete mathematical formulations and calculation parameters for the CWT methodology are detailed in Text S1.~~It can efficiently and accurately determine the transport trajectories of different pollutants, and then classify and aggregate the backward trajectories during the study period through the Euler clustering method, and output air mass trajectories with different proportions. In this study, the HYSPLIT model was used to identified backward trajectories of Xinxiang during the period from 2021 to 2023. The model inputs hourly meteorological data from the Global Data Assimilation System (ftp://arlftp.arlhq.noaa.gov/pub/archives/gdas1). Taking the starting point (central location of Xinxiang: 35.30°N, 113.88°E) as a reference, 48 hour backward trajectories terminating at 100 m above ground level were calculated for study period.~~

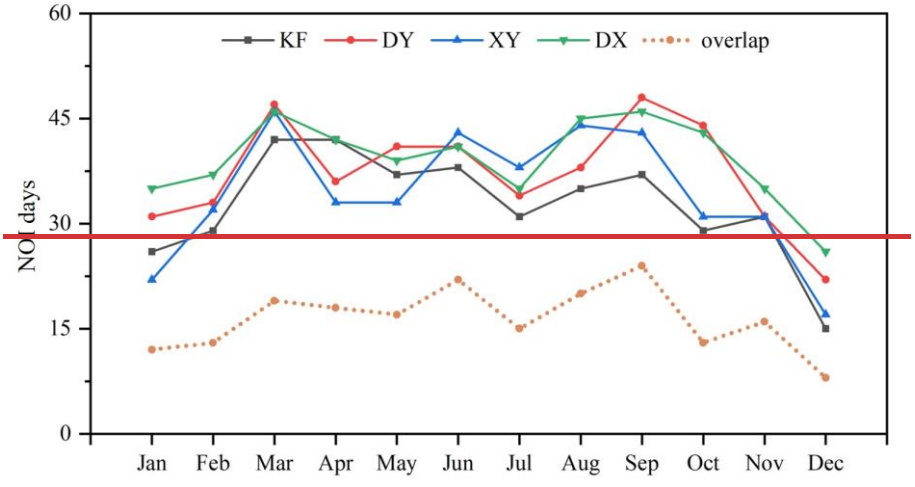
~~Using air mass trajectories, we can interpolate $O_3$ concentrations and then apply concentration weighted trajectory (CWT) analysis to identify potential source regions and contributions of $O_3$ in Xinxiang (Shi et al., 2024; Wang et al., 2024). Detailed information is available in Text S1.~~

## 3 Results and discussion

### 3.1 Characteristics of NOI days

#### 3.1.1 Temporal variation of NOI days and NOI occurrence time

Fig. 1 illustrates the monthly variation of NOI days at national monitoring stations in Xinxiang from 2021 to 2023. The DX station recorded the highest cumulative NOI days (~~470~~ 444 days), while KF exhibited the lowest frequency (~~392~~ 370 days). Additionally, all stations showed similar monthly variation trends: NOI days progressively increased from January to March, peaking in March (42-47 days), and then maintained high-level fluctuations from April to September. ~~(reaching a secondary peak in September (37-48 days))~~ Notably, a distinct secondary peak is observed in June (Fig. 1). This early summer peak can be primarily attributed to the coupled effects of seasonal meteorological shifts and $O_3$ precursor dynamics. Meteorologically, June marks the transition to summer in the NCP, characterized by sharp increases in temperature and intensified solar radiation. Concurrently, these warmer conditions significantly stimulate the enhanced emissions of natural $O_3$ precursors (e.g., biogenic VOCs). The combination of abundant precursors and highly favorable meteorological conditions drives intense daytime photochemical $O_3$ production. This vigorous daytime accumulation generates a highly concentrated $O_3$ residual layer by dusk, which ultimately acts as an abundant aloft source for NOI events. Subsequently, the frequency reaches another peak in September (32-44 days) before declining~~, and declined~~ sharply from October to December, reaching annual minima (15-26 days). This indicated that warm seasons favor NOI occurrence. However, it is crucial to emphasize that a high regional $O_3$ background does not trivially dictate the occurrence of NOI. While the warm season provides a highly concentrated aloft reservoir, the actual occurrence of an NOI event (which must vigorously overpower the intense local nocturnal NO titration typical of urban environments) strictly requires the concurrent presence of specific dynamic meteorological triggers.



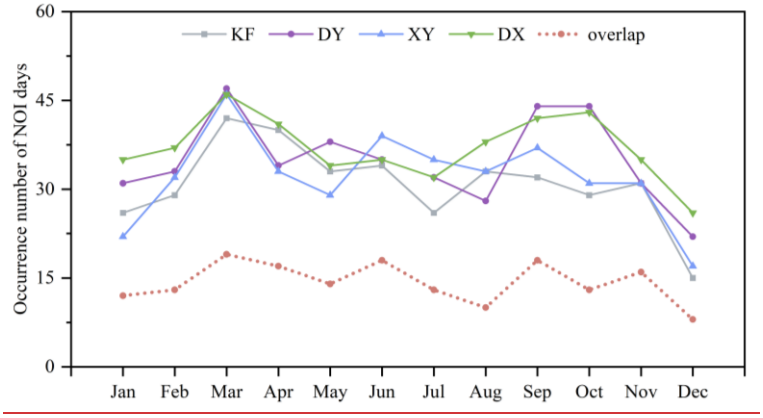



**Figure 1: Monthly variation of NOI days at national monitoring stations in Xinxiang, 2021-2023 (overlap: representative NOI days with completely coincident dates across the four stations).**

Fig. S3 further demonstrates monthly variations of NOI occurrence time. ~~Type A~~LN dominated with ~~71.35~~69.53% occurrence frequency across all months, followed by ~~Type B~~EN (~~19.76~~21.69%) and ~~Type C~~WN (~~8.89~~8.78%). This indicated that NOI events in Xinxiang tended to occur from 00:00 to 06:00 LT compared with those occurring between 20:00 and 23:00 LT. From a boundary-layer dynamics perspective, the absolute dominance of post-midnight events (LN) indicates that most NOI occurs when the nocturnal surface inversion is fully established and highly stable. Consequently, triggering these events requires substantial active mechanical forcing (e.g., intense wind shear or subsidence) capable of breaking this deep stability, which directly motivates the detailed synoptic and dynamical mechanism analysis in Sections 3.3 and 3.4.

Furthermore~~Notably~~, ~~Type A~~LN generally increased from March to September (68.24-80.60~~69.28-82.67~~%) compared with other months (60.54-67.50%), while ~~Type B~~EN exhibited an opposite trend (Fig. S3). This reflected that warm seasons, characterized by richer daytime $O_3$ accumulation in the residual layer, would intensify the occurrence frequency of LN.~~This reflected that warm seasons would intensify the occurrence of Type A.~~

### 3.1.2 Impact of NOI occurrence time on $O_3$ levels

~~Given the significant temporal variation characteristics of NOI days and NOI occurrence time, different occurrence time of NOI may have potential differential impacts on $O_3$ levels. Therefore, we further analyzed $O_3$ diurnal variations of NOI days under different NOI occurrence time in different seasons (Fig. 2). In spring, compared with EN, LN exhibited higher initial $O_3$ concentrations before 12:00 LT but lower afternoon peaks. This difference is likely attributable to lower temperature and solar radiation in LN (Hu et al., 2021). In other seasons, LN consistently showed both higher initial $O_3$ concentrations and peaks than EN, indicating generally higher $O_3$ levels in LN. Moreover, except that EN and WN exhibited comparable $O_3$ levels in spring and summer, WN displayed higher $O_3$ concentrations than EN in other seasons. This indicated that compared with LN and WN, EN exhibited the lowest overall $O_3$ levels, which also meant that the meteorological conditions of EN were not conducive to the formation or accumulation of $O_3$. Overall, the average $O_3$ concentrations followed: LN (82.64 μg m$^{-3}$) > WN (75.04 μg m$^{-3}$) > EN (66.46 μg m$^{-3}$). We hypothesized that these differences in NOI days may be associated with types of~~

~~meteorological conditions, as different seasons often featured distinct weather activities, which served as critical factors triggering NOI.~~

Given the significant temporal variation characteristics of NOI days, different occurrence times may exert distinct impacts on the overall $O_3$ diurnal cycle. Therefore, we further analyzed the $O_3$ diurnal variations on NOI days categorized by their occurrence time across different seasons (Fig. 2). Notably, in winter, compared with EN, LN exhibited higher initial $O_3$ concentrations at the onset (around 18:00 LT), but maintained slightly lower levels throughout the late night and morning hours. This dampened afternoon peak is likely a direct consequence of this lower morning baseline. In winter, when daytime photochemical production is inherently limited, the maximum absolute $O_3$ concentration heavily depends on the morning carry-over levels. Consequently, starting from a lower morning baseline naturally constrains the subsequent afternoon peak. In contrast, across all other seasons (spring, summer, and autumn), LN consistently showed both higher nocturnal/morning $O_3$ concentrations and higher afternoon peaks than EN, indicating a generally more intense overall $O_3$ pollution burden associated with LN events. Furthermore, except for autumn where EN and WN exhibited comparable $O_3$ levels, WN generally displayed higher $O_3$ concentrations than EN in other seasons. This indicates that EN exhibited the lowest overall $O_3$ levels among the three categories, implying that the meteorological conditions triggering EN are relatively the least conducive to overall $O_3$ accumulation. Overall, the total average $O_3$ concentrations followed the order: LN (78.68 μg $m^{-3}$) > WN (76.82 μg $m^{-3}$) > EN (71.14 μg $m^{-3}$). We hypothesize that these temporal discrepancies are intrinsically linked to the distinct evolutionary characteristics of specific weather types, which serve as the primary physical triggers modulating both the timing and varying intensities of NOI events.

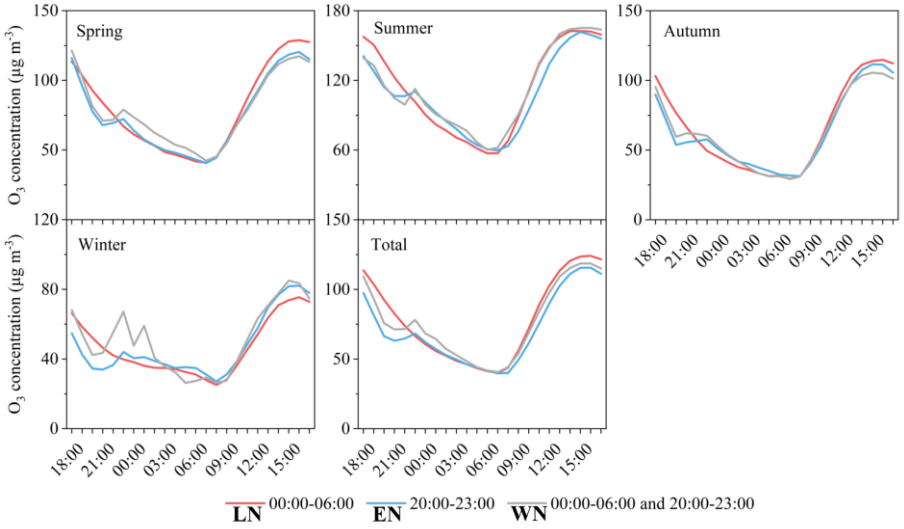



**Figure 2: $O_3$ diurnal variations of NOI days under different NOI occurrence time in different seasons.**

Given the discrepancy in the occurrence dates of NOI days in different stations in Xinxiang, standardizing the dates of local NOI days is essential to investigate the weather type characteristics of NOI days. We established unified occurrence dates

through cross-analysis of multi-station data (Fig. ~~S5~~3), and found that KF, XY, DX, and DY had ~~197~~ 171 NOI days occurring on the same days during 2021-2023 in Xinxiang. Thus, these ~~197~~ 171 NOI days were selected as representatives to characterize the overall occurrence of local NOI days. ~~Notably, the monthly variation characteristics of representative NOI days were highly consistent with those observed at the four stations individually (Fig. 1). This indicated that the representative NOI days could effectively reflect the occurrence of NOI days in Xinxiang and were scientifically valid.~~It is worth noting that non-overlapping NOI events frequently occur among the different stations, highlighting the inevitable influence of random localized emission noise and uncoordinated micro-environmental fluctuations. To rigorously isolate the overarching synoptic-scale meteorological drivers from these random local chemical/emission noises, this study specifically focused on representative events where NOI occurred simultaneously across all stations. Rather than neglecting local boundary-layer processes, these simultaneous occurrences serve as robust indicators of powerful regional episodes. They demonstrate that the large-scale synoptic forcing was sufficiently intense to synchronize the local boundary-layer dynamics (e.g., vertical wind shear and turbulent mixing) across the entire urban region. This rigorous screening ensures that the localized physical mechanisms evaluated in subsequent sections are systematically driven by macro-weather types, rather than coincidental local perturbations. Furthermore, the monthly variation of these representative regional events (indicated by the "overlap" dotted line in Fig. 1) consistently matches the seasonal trends observed at individual stations (e.g., distinct peaks in March and September, and dips in January and December). This indicated that the representative NOI days could effectively reflect the occurrence of NOI days in Xinxiang and were scientifically valid.

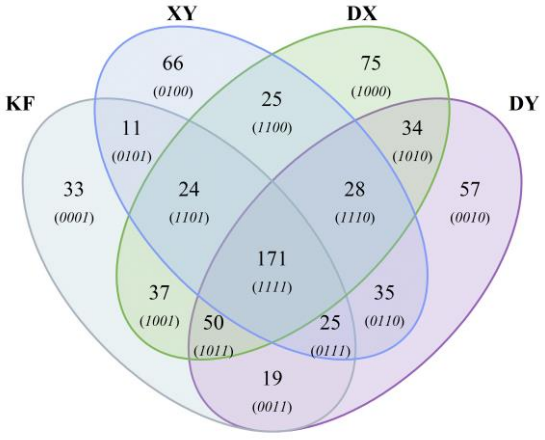



**Figure 3: Overlapping occurrences of NOI days at national monitoring stations in Xinxiang, 2021-2023. The four-digit binary codes in parentheses indicate the specific occurrence status of NOI events across the four stations (in the order of DX, XY, DY, and KF). A digit of 1 represents the occurrence of the event, and 0 represents non-occurrence (e.g., (1111) denotes cooccurrence at all four stations, while (1000) denotes occurrence only at the DX station).**

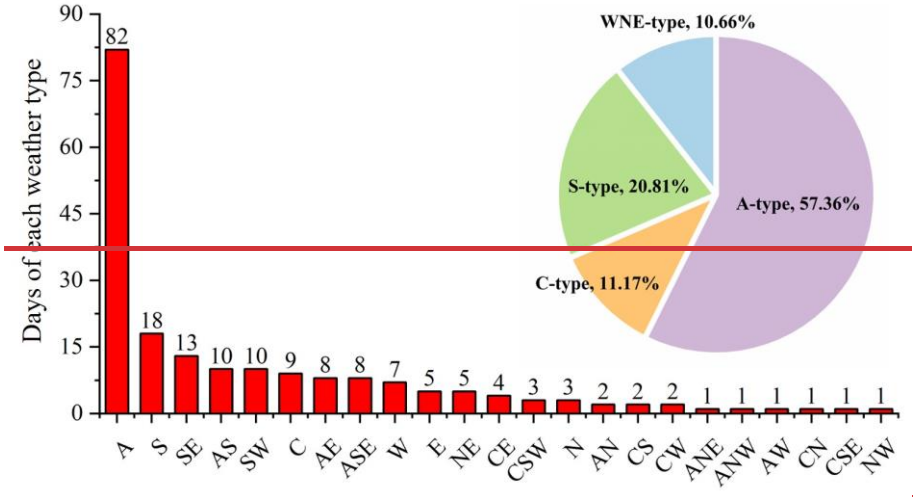
### 3.2 Weather types of representative NOI days

The Lamb-Jenkinson synoptic circulation classification method was utilized to categorize weather types for representative NOI days. The categorization results are presented in Table S1. ~~23~~ 20 weather types were identified from ~~197~~ 171 representative NOI days, including 2 vorticity types (named A and C), 8 directional types (including S, SE, SW, W, NW, N, NE and E) and ~~13~~ 10 hybrid types (named AE, ~~AN,~~ ANE, ~~ANW,~~ AS, ASE, ASW, ~~CE,~~ CN, CS, CSE, CSW and CW). Among them, vorticity types accounted for ~~46.19~~49.12% of the total, with anticyclonic type A alone contributing ~~82~~ 77 days. Directional and hybrid types accounted for ~~31.47~~33.92% and ~~22.34~~16.96%, respectively. Fig. ~~S6~~ S4 displays the mean SLP of representative NOI days under different weather types from 2021 to 2023. It can be seen that the position of high- and low-pressure centers exhibit certain discrepancies among different weather types. Furthermore, to explicitly validate that this SLP-based classification accurately captures airflow characteristics in lower troposphere, Fig. S5 illustrates the spatial distributions of mean SLP overlaid with 850 hPa wind fields for the 20 identified weather types. The spatial patterns demonstrate a high degree of physical consistency, wherein the surface pressure gradients align with the 850 hPa wind field. This confirms that the SLP-based Lamb-Jenkinson method is highly robust and effectively represents synoptic circulation background of upper boundary-layer.

Liu et al. (2019) noted that northern China is frequently affected by large-scale weather systems such as the Yellow River cyclone, the Siberian high, and the Western Pacific subtropical high. These interactions induce frequent shifts in weather classifications and the seasonal migration of high- and low-pressure centers, resulting in distinct monthly meteorological patterns. According to the position of central system and different meteorological elements of each classification, the ~~23~~ 20 weather types were classified into four primary weather types: (1) A-type (weather types related with high-pressure), including A, AE, ~~AN,~~ ANE, ~~ANW,~~ AS, ASE and ASW; (2) C-type (weather types related with low pressure), including C, ~~CE,~~ CN, CS, CSE, CSW and CW; (3) S-type (geostrophic wind direction to the south), including S, SE and SW; (4) WNE-type (geostrophic wind direction between west-north-east), including W, NW, N, NE and E. Fig. ~~2~~ 4 illustrates the proportion of four primary weather types and the days of each weather type. As shown in Fig. ~~2~~4, representative NOI days predominantly occurred under A-type weather types (~~113~~ 99 days, 57.~~36~~89% of the total), followed by S-type (~~41~~ 34 days, ~~20.81~~19.88%), ~~C~~WNE-type (~~22~~ 24 days, ~~11.17~~14.04%), and ~~WNE~~C-type (~~21~~ 14 days, ~~10.66~~8.19%). These findings indicated that the meteorological conditions of A-type were most conducive to the occurrence of NOI days.

Notably, to extract the overarching dynamical mechanisms and reduce the statistical noise of the 20 specific Lamb-Jenkinson weather types, we quantitatively clustered them into four major archetypes: Anticyclonic (A-type), Cyclonic (C-type), Southerly (S-type), and West-North-East (WNE-type). Rather than subjective grouping, this clustering was rigorously based on their shared physical topology: specifically, the polarity of SLP anomalies, geostrophic vorticity, and the primary azimuth of geostrophic wind vectors. The detailed quantitative criteria for each of the four weather types are provided in Text S2. To further validate the physical distinctness of this categorization, composite analysis of the synoptic fields and Analysis of Variance (ANOVA) on localized boundary layer variables were conducted.

To verify that the four grouped weather types possess fundamentally distinct atmospheric backgrounds, we analyzed their composite mean SLP and 850 hPa wind fields (Fig. 5). The spatial distributions unequivocally demonstrate distinct synoptic forcings: A-type is dominated by a strong, uniform high-pressure center over the study region (Fig. 5(a)); C-type is characterized by cyclonic curvature and low-pressure system (Fig. 5(b)); S-type is driven by intense southerly advection between a western low and an eastern high (Fig. 5(c)); and WNE-type features strong northeasterly flows driven by a massive continental high to the northwest (Fig. 5(d)). Furthermore, to statistically confirm that these different synoptic structures translate into distinctly different local thermodynamic environments, a One-Way ANOVA was performed on the nocturnal anomalies of key meteorological variables (T, RH, WS, PBLH and $U^*$) across the four groups. The resulting statistical distributions and data spreads are visually compared in Fig. 6, while the precise quantitative parameters and significance test results are detailed in Table S2. To strictly isolate the meteorological perturbations driven by synoptic systems and to eliminate the influence of seasonal and interannual backgrounds, the nocturnal anomalies ($\Delta$) for key meteorological variables were calculated as the difference between the NOI days' specific nocturnal average and the corresponding monthly nocturnal mean. The results show that the inter-group differences are highly statistically significant (all $p < 0.01$), definitively proving that our quantitative classification objectively separates fundamentally different boundary layer environments.



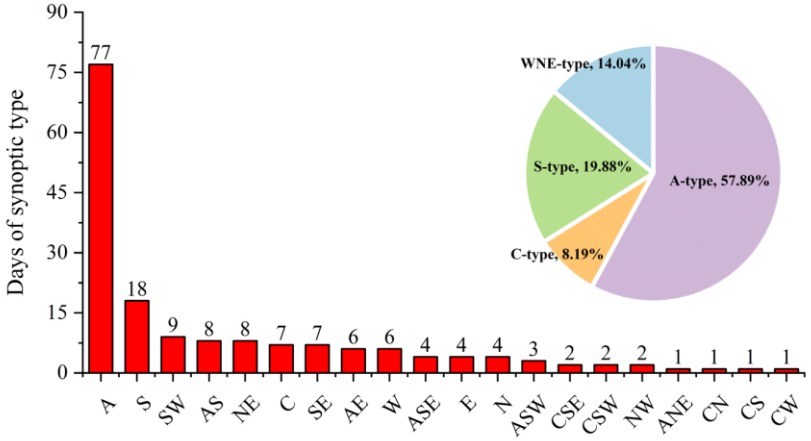
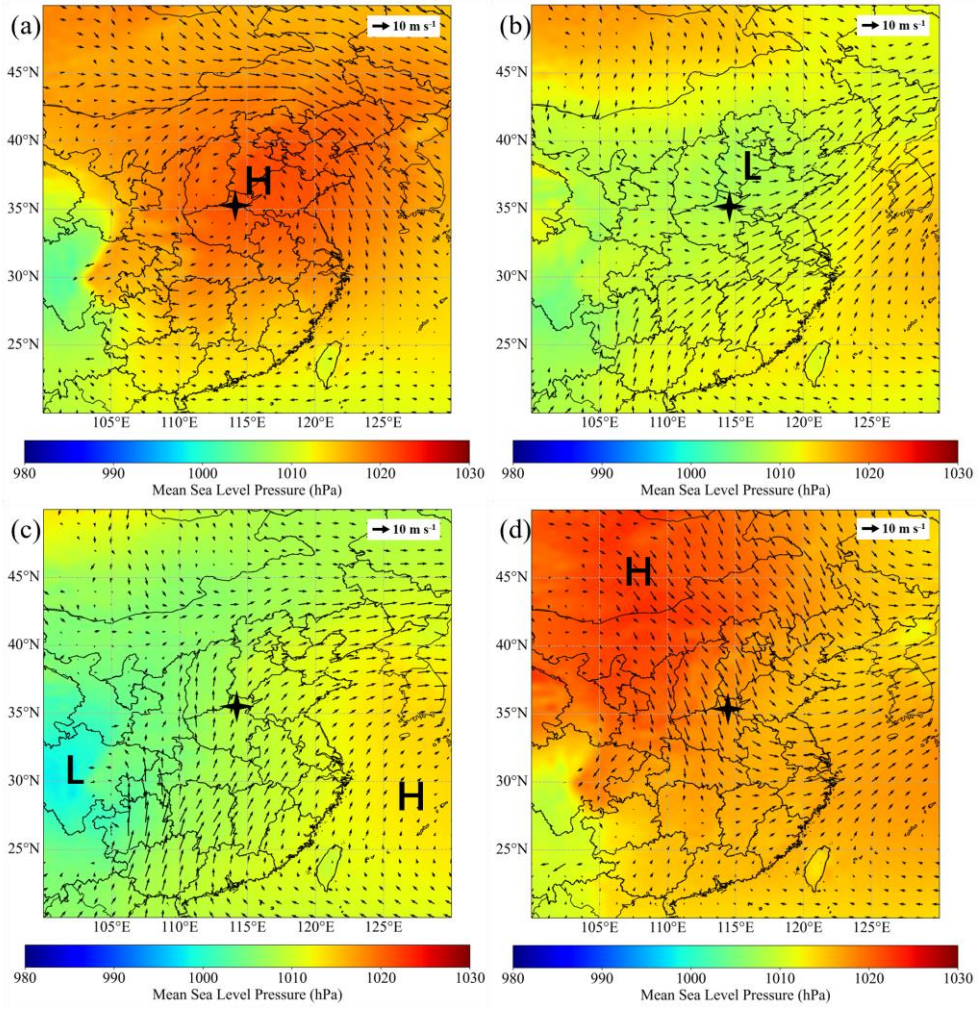



**Figure ~~2~~4: Proportion of four primary weather types and days of each weather type during representative NOI days in Xinxiang, 2021-2023.**

~~Owing to the pronounced differences in meteorological characteristics among seasons in Xinxiang, the occurrence frequencies of various weather types are affected. Thus, we analyzed the seasonal variations of the four primary weather types (Fig. S7). A-type predominantly occurred in autumn (38 days), followed by summer (28 days), winter (24 days), and spring (23 days). Both C-type and S-type exhibited higher frequencies in spring and summer and lower occurrences in autumn and winter. Unlike the other three weather types, WNE-type showed relatively consistent frequencies across seasons, generally 5–6 days. Overall, the four primary weather types exhibited significantly different seasonal variation patterns.~~




360 **Figure 5: Spatial distribution of composite mean SLP and 850 hPa wind fields under different weather categories: (a) A-type, (b) C-type, (c) S-type, (d) WNE-type (asterisk indicates the location of Xinxiang; "H" and "L" stand for high-pressure and low-pressure, respectively).**

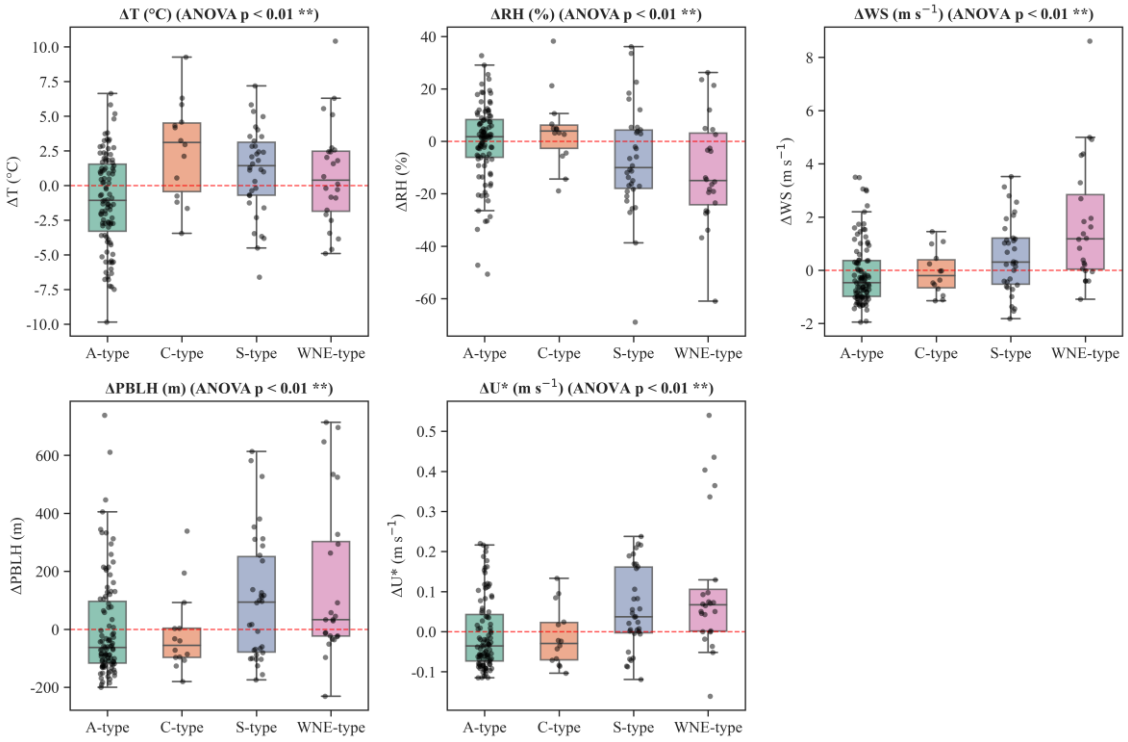



**Figure 6: One-Way ANOVA results for key meteorological variables (T, RH, WS, PBLH and U*) of different synoptic categories. In each boxplot, the central black solid line indicates the median. The horizontal red dashed line denotes the zero-anomaly reference.**

### 3.3 Meteorological characteristics of primary weather types

As established in Section 3.1, the vast majority of NOI events in Xinxiang occur during the LN period. During this phase, the nocturnal boundary layer is characterized by a fully established surface inversion, creating a highly stable thermodynamic environment. To trigger downward $O_3$ transport under such extreme stability, localized residual turbulence is entirely insufficient. Instead, it requires massive, active mechanical forcing capable of physically breaking the inversion layer. Because such powerful mechanical triggers are fundamentally governed by macro-scale weather systems, identifying the specific synoptic circulations is the critical next step to unravel the forcing mechanisms behind these NOI events.

It should be noted that while seasonal variations significantly influence the daytime photochemical generation and absolute background concentrations of $O_3$, the nocturnal occurrence of NOI is predominantly driven by physical transport. As validated by the seasonal comparison (Fig. S6 and Text S3), while the absolute intensity of meteorological variables naturally fluctuates across seasons, the fundamental dynamical frameworks for a given weather type (e.g., the general orientation of horizontal pressure gradients and patterns of vertical motions) maintain functionally comparable mechanical triggers. Therefore, rather than focusing on seasonal background variations, our study focuses on elucidating these primary, synoptically-driven local meteorological drivers that trigger NOI.

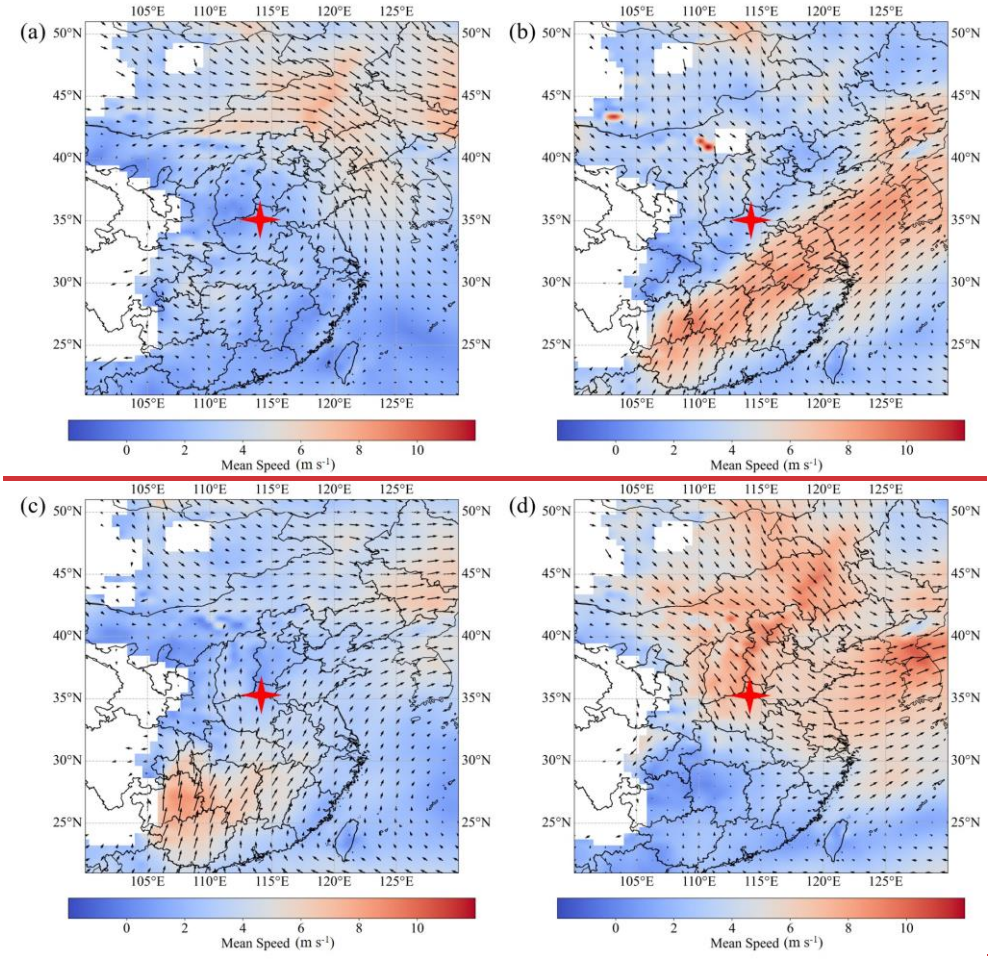
The representative NOI days in Xinxiang were classified into four weather types (A-type, C-type, S-type, and WNE-type), with each exhibiting distinct meteorological features. Fig. 7 ~~Figs. S8 and 3~~ illustrates the spatial distributions of ~~SLP and~~ 850 hPa wind fields under four weather types. Under A-type, Xinxiang was located near a high-pressure center, with an outward-rotating wind field at 850 hPa (Figs. 5(a) and 7(a)), indicating the presence of an anticyclonic high-pressure system. Driven by this synoptic forcing, Xinxiang experienced extremely calm conditions. As explicitly demonstrated by the nocturnal anomalies in Fig. 6 and Table S2, A-type was characterized by negative anomalies in wind speed (mean: $\Delta WS$ = -0.10 m $s^{-1}$) and friction velocity (mean: $\Delta U^*$ = -0.01 m $s^{-1}$), alongside a strongly constrained boundary layer (mean: $\Delta PBLH$ = 3.56 m, representing negligible expansion). This indicates that the overriding high-pressure system creates a highly stable environment. The explicit intrusion process of $O_3$ under this subsidence will be further verified in Section 3.4.

Under C-type, Xinxiang was dominated by low-pressure systems (Fig. 5(b)). At 850 hPa, a strong airflow originating near the coastal region of Guangxi Province moved continuously northeastward (Fig. 7(b)). This airflow not only moved at a high speed, but also likely carried substantial moisture, significantly enhancing atmospheric instability in its trajectory and surrounding regions (including Xinxiang), intensifying convective activity, and increasing the risk of heavy rainfall. Combined with the water vapor flux and divergence fields at 850 hPa, we find that the intense southwest warm-wet moisture transport belt under C-type is extremely prominent. Significant moisture convergence is observed along the entire path of this belt (including Xinxiang) (Fig. S7). Notably, the local meteorological anomalies perfectly capture this advection, with C-type uniquely coinciding with distinct positive anomalies in temperature (mean: $\Delta T$ = 2.60 °C) and the highest relative humidity anomaly among all weather types (mean: $\Delta RH$ = 4.08%). This localized warm and highly humid environment, dynamically coupled with a cyclonic low-pressure background, significantly amplifies atmospheric thermodynamic instability, highly favoring the development of regional convection and precipitation. Consequently, rather than uniform large-scale subsidence, NOI under C-type is primarily triggered by convective motions and the subsequent development of cold pools.

S-type represents a dynamic environment driven by distinct horizontal advection. Under S-type, Xinxiang was situated in a tight pressure gradient, typically between a western low and an eastern high (Figs. 5(c) and 7(c)). Driven by this synoptic setup, continuous southerly geostrophic winds prevailed over the region. As detailed in Table S2, S-type produced significant positive anomalies in local wind speed (mean: $\Delta WS$ = 0.54 m $s^{-1}$) and friction velocity (mean: $\Delta U^*$ = 0.06 m $s^{-1}$). These specific values rigorously demonstrate that beyond facilitating regional horizontal transport (which will be explicitly traced in Section 3.4.1), the southerly advection directly generates substantial localized mechanical turbulence at the surface, physically lifting the nocturnal boundary layer (mean: $\Delta PBLH$ = 102.41 m). This localized mechanical shear serves as the direct trigger for breaking nocturnal stability, subsequently entraining $O_3$-rich air from the elevated residual layer down to the surface and triggering NOI events.

Although Xinxiang often featured a massive continental high-pressure system (e.g., the Siberian High) to the northwest under WNE-type (Fig. 5(d)), their local dynamics are fundamentally different from the pure subsidence of A-type. At 850 hPa, the region was obviously influenced by a northwestern airflow (Fig. 7(d)), consistent with the geostrophic wind characteristics of WNE-type. Unlike A-type, where the study area sits calmly at the high-pressure center, under WNE-type, Xinxiang was located

at the densely packed periphery of the advancing high. Consequently, the macroscopic forcing shifts to intense horizontal pressure gradients (Figs. 5(d) and 7(d)). This kinematic distinction is perfectly captured by the localized surface anomalies (Table S2). WNE-type exhibited the most extreme positive anomalies among all categories, with local wind speed (mean: $\Delta WS = 1.74$ m s$^{-1}$) and friction velocity (mean: $\Delta U^* = 0.11$ m s$^{-1}$) far exceeding other types. Driven by this intense horizontal advection and wind shear, the nocturnal boundary layer experienced massive mechanical lifting (mean: $\Delta PBLH = 156.22$ m). Furthermore, this intense mechanical mixing effectively breaks the nocturnal surface inversion, bringing slightly warmer air from aloft downward (detailed mechanism analysis is presented in Section 3.4.2). This vigorous downward mixing of the elevated residual layer shares conceptual similarities with the nocturnal fumigation-like processes documented in other literature (Wu et al., 2023; He et al., 2022), which also explains the observed positive temperature anomaly (mean: $\Delta T = 0.77$ °C). Therefore, despite the high-pressure background, it is this extraordinarily strong localized shear and turbulent mixing, that serves as the primary mechanical driver forcing $O_3$ downward to the surface during WNE-type. Combined with rapid dispersion of local NO emissions under high winds that greatly mitigates nighttime titration, vigorous vertical entrainment counteracts both horizontal diffusion and titration loss of $O_3$, and ultimately causes a net $O_3$ surge.


(a)
(b)
(c)
(d)
105°E
110°E
115°E
120°E
125°E
50°N
45°N
40°N
35°N
30°N
25°N
0
2
4
6
8
10
Mean Speed (m s-1)

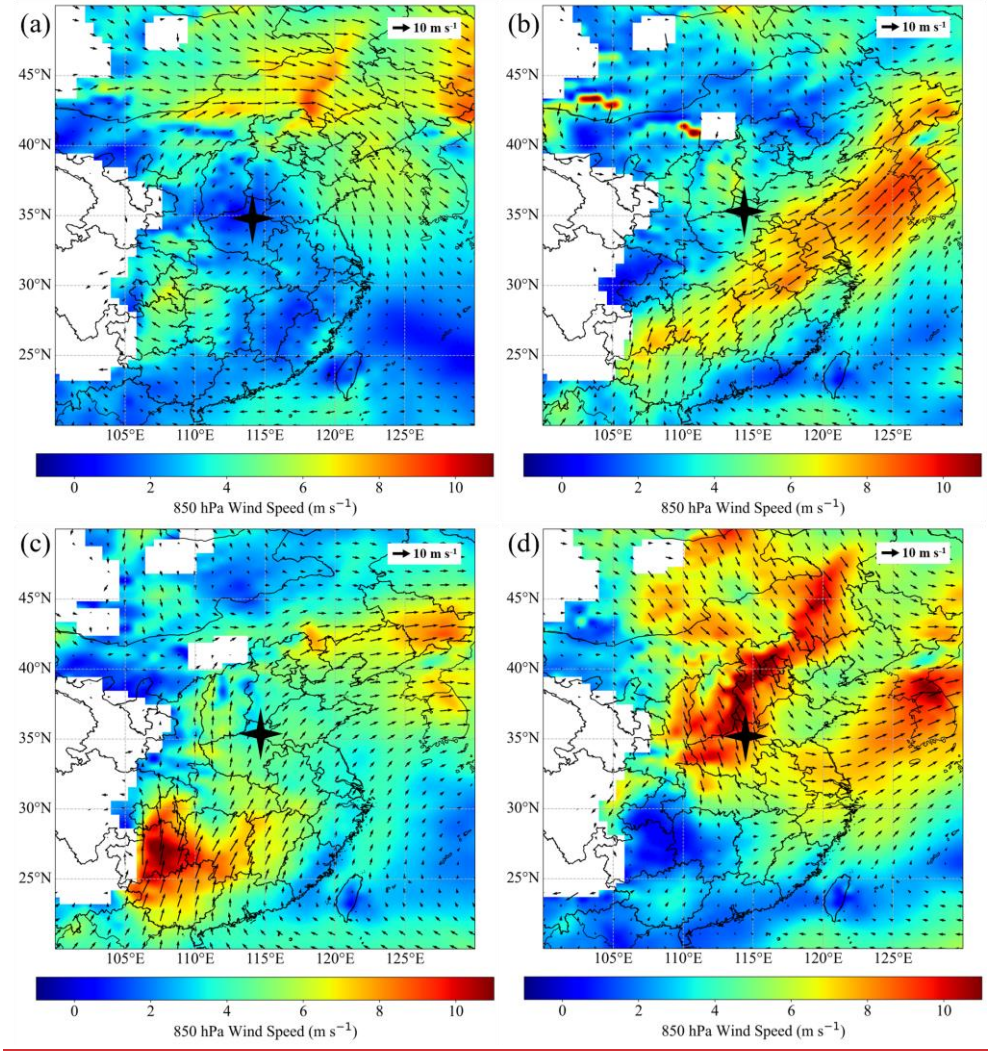



**Figure ~~3~~7: Spatial distribution of wind field at 850hPa under different weather types: (a) A-type, (b) C-type, (c) S-type, (d) WNE-type (asterisk indicates the location of Xinxiang).**

~~Under A-type, Xinxiang was located near a high-pressure center, with an outward-rotating wind field at 850 hPa (Figs. S8(a) and 3(a)), indicating the presence of an anticyclonic high-pressure system. Controlled by this system, surface observations showed the average temperature of 15.53 °C, relative humidity of 64.31%, and wind speed of 2.75 m s$^{-1}$ (Table S2), reflecting a mild, dry, and moderately windy environment. In Section 3.2, we found that A-type occurred most frequently in autumn. Table S3 displays the average temperature, relative humidity, wind speed, wind direction and precipitation observed on the ground in Xinxiang under four weather types in different seasons. In autumn, A-type exhibited the average temperature of 15.71 °C and relative humidity of 65.46%, representing intermediate conditions between the high temperature and humidity of summer and the low temperature and humidity of winter. These moderate conditions favored the stability of the anticyclonic high-pressure system (Holton and Hakim, 2013). Additionally, autumn in northern China was a transitional season with~~

relatively stable atmospheric circulation, influenced by the Siberian high (Chen et al., 2023), which further supported the formation of A-type conditions.

In contrast, other seasons presented unfavorable weather conditions for the maintenance of A-type. Summer was characterized by high temperature (23.63 °C) and humidity (73.73%), with vigorous convective activities that easily triggered low-pressure systems (Yihui and Chan, 2005). Winter featured low temperature (5.98 °C), and was often affected by the frequent southward movement of cold air, resulting in rapid changes in weather systems (Zhang et al., 1997b). Spring was marked by unstable atmospheric circulation and frequent frontal activities (Wang et al., 2023c). All these factors hindered the maintenance of high-pressure anticyclones.

Contrasting with A-type, Xinxiang under C-type was dominated by low-pressure systems (Fig. S8(b)). At 850 hPa, a strong airflow originating near the coastal region of Guangxi Province moved continuously northeastward (Fig. 3(b)). This airflow not only moved at a high speed, but also likely carried substantial moisture, significantly enhancing atmospheric instability in its trajectory and surrounding regions (including Xinxiang), intensifying convective activity, and increasing the risk of heavy rainfall. Under the influence of this airflow, Xinxiang experienced significant changes in weather conditions. According to Table S2, the average surface temperature (19.30 °C) and relative humidity (72.43%) under C-type in Xinxiang were higher, and it also had the highest average precipitation (0.49 mm $h^{-1}$) among the four weather types, which further implied frequent rainfall activities in C-type.

Additionally, C-type primarily occurred in spring and summer, when the East Asian monsoon strengthened. During this period, warm-moist air masses from southern China were transported northward (Yihui and Chan, 2005), supplying abundant moisture to Xinxiang (average relative humidity and precipitation: 72.77%, 0.325 mm $h^{-1}$ in spring and 75.39%, 0.944 mm $h^{-1}$ in summer). The convergence of warm-moist air with cold air facilitated the formation of low-pressure systems (You and Ting, 2021), promoting the occurrence of C-type. Furthermore, high average surface temperatures in spring (20.70 °C) and summer (23.26 °C) enhanced surface heating, atmospheric instability, and convection, providing dynamic conditions for the development of low-pressure systems and the occurrence of heavy rainfall (Yihui and Chan, 2005; Li et al., 2021). Compared with spring and summer, winter was often affected by cold air, with relatively stable atmospheric circulation (Zhang et al., 1997a), low temperature and humidity (8.79 °C and 56.75%, respectively). Although autumn had high humidity level (73.77%), the temperature was low (6.86 °C), and the atmospheric stability was strong, with weaker convective activities (Eom and Myoung-Seok, 2011). These factors were not conducive to the formation and maintenance of low-pressure systems.

Unlike A-type and C-type, S-type and WNE-type were primarily associated with geostrophic wind direction. Under S-type, Xinxiang was located at the junction of the edges between high- and low-pressure (Fig. S8 (c)), indicating that the region was influenced by two different weather systems and thus experienced more frequent weather changes. At 850 hPa, Xinxiang was clearly affected by a southern airflow (Fig. 3(c)), which was consistent with the southern geostrophic wind characteristic of S-type. Ground observations showed that the average wind speed and direction under S-type in Xinxiang were 2.53 m $s^{-1}$ and 136.77 ° (Table S2). The wind direction belonged to the southeast wind, indicating that the surface wind was basically similar to the geostrophic wind.

~~S-type occurred most frequently in spring and summer, followed by autumn and winter. This seasonal variation resulted from multiple factors. In spring and summer, the northward shift of the Western Pacific subtropical high facilitated collisions between southern warm-moist airflow and cold air masses from the north. This formed frontal convergence zones (high- and low-pressure transition belts) and influenced the southern geostrophic wind in Xinxiang (Yihui and Chan, 2005). During these two seasons, the sun heated the surface, forming a thermal low-pressure area. In coordination with the subtropical high aloft, a vertical pressure gradient with "high-pressure aloft and low-pressure near the surface" was formed (Li et al., 2021). Superimposed with the topography influence of Taihang Mountain, the low-pressure disturbances would be intensified, further contributing to the stable maintenance of the southern geostrophic wind (Xia and Zhang, 2019; Xu and Yao, 2015). Unlike spring and summer, during autumn, the subtropical high retreated southward, and cold air activity increased, significantly shortening the influence duration of transition belts (Eom and Myoung-Seok, 2011). In winter, Xinxiang was controlled by the cold high-pressure system, and the transition belts disappeared (Zhang et al., 1997a). All these factors inhibited the development of the southern geostrophic wind.~~

~~Under WNE type, Xinxiang was controlled by a high pressure system (Fig. S8(d)). At 850 hPa, the region was obviously influenced by a northwestern airflow (Fig. 3(d)), consistent with the geostrophic wind characteristics of WNE type. Notably, the average surface wind speed and direction under WNE type in Xinxiang were 2.78 m $s^{-1}$ and 171.98 ° (Table S2). There was a large deviation between this wind direction and the geostrophic wind, which was mainly attributed to the significant influence of factors such as friction, terrain, and local weather systems on the surface wind (Li et al., 2020a).~~

~~Additionally, WNE type occurred with comparable frequency among all seasons, which was essentially attributable to the combined influence of geographic location, multi-scale circulation systems, and terrain. Xinxiang was situated within the convergence zone where the cold high pressure, the western Pacific subtropical high, and transient migratory ridges interacted (Yihui and Chan, 2005). Although the high pressure systems dominated in different seasons had various thermal driving mechanisms, they all formed a wind field between the west-north-east direction through the geostrophic balance (Zhang et al., 1997a). Furthermore, the eastern foothills of the Taihang Mountain exerted a stabilizing dynamic influence on local circulation (Xia and Zhang, 2019; Xu and Yao, 2015). The combined effect of weather systems and topographic dynamic forcing ultimately resulted in no significant seasonal differences in the frequency of WNE type.~~

### 3.4 Physical ~~Formation~~ mechanisms of NOI days under different weather types

#### 3.4.1 ~~Regional transport~~3D regional transport and synoptic subsidence

~~To explore the triggering factors for the formation of NOI days in Xinxiang under the four different weather types, this study delved deeply into the regional and vertical transport processes. The backward trajectories for Xinxiang under the four weather types are shown in Figs. S9. The spatial distributions of CWT are illustrated in Fig. 4. Under A type, air masses reaching Xinxiang predominantly originated from the north-northeast direction (64.75%), with a minor contribution from the south-southeast direction (20.91%) (Fig. S9(a)). These two trajectories moved slowly towards Xinxiang. During A type, the potential~~

~~source areas of high $O_3$ levels were mainly distributed in the central and eastern Henan, western Shandong, and northern Anhui (WCWT values: 90-100 μg $m^{-3}$) (Fig. 4(a)). When the transport trajectories passed over these high-value areas, they carried high-concentration pollutants to the target region. Under C-type, the east direction (46.97%) served as the dominant airflow channel, with short trajectories and slow movement speeds (Fig. S9(b)). This indicated that the pollution transport was mainly influenced by adjacent regions, while the slow movement prolonged the pollutant residence time, increasing the risk of local $O_3$ accumulation. During this period, the high-value areas of $O_3$ were concentrated in the central and northern Henan and the border region between Hebei and Shandong (WCWT ≈ 100 μg $m^{-3}$) (Fig. 4(b)), facilitating the transport of high-concentration $O_3$ or precursors to Xinxiang.~~

~~Influenced by the geostrophic wind, during S-type, the airflow trajectories from the south direction were dominant, contributing 46.34% to the total trajectories (Fig. S9(c)). The high value areas of $O_3$ during this period were distributed on both the north and south sides of Xinxiang, with the southern side covering and extending the widest area, mainly including the Central China urban agglomeration (WCWT > 100 μg $m^{-3}$) (Fig. 4(c)). These $O_3$ and precursors from southern regions converged and uplifted at the foothills of the Taihang Mountain, exacerbating the local $O_3$ levels in Xinxiang. Under WNE-type, airflow trajectories were essentially within the W-N-E range (Fig. S9(d)). The potential source regions of high $O_3$ levels were limited to central and northern Henan, displaying lower WCWT values (70-80 μg $m^{-3}$) compared with other weather types (Fig. 4(d). This indicated that although WNE-type was influenced by adjacent regions, the overall transport intensity was relatively weak.~~

To explore the triggering factors for the occurrence of NOI days under the four weather types, we investigated the 3D regional backward trajectories and CWT spatial distributions (Figs. 8, 9 and S8). While horizontal advection determines the regional source regions, the vertical profiles of these trajectories provide crucial Lagrangian evidence of downward transport.

Under A-type, air masses predominantly originated from the north (58.69%) (Fig. 8(a)). Crucially, the 3D altitude profiles (Fig. S8(a)-(b)) reveal that these dominant clusters originated from significantly high altitudes (~800 hPa) 48 hours prior, exhibiting continuous and massive subsidence as they approached Xinxiang. When these subsiding trajectories passed over the high $O_3$ potential source areas in northern Henan and western Shandong (CWT: 90-100 μg $m^{-3}$; Fig. 9(a)), regions well-documented for their heavy industrial facilities and intense precursor emissions (Lu et al., 2019; Li et al., 2019), they effectively entrained $O_3$-rich air from the residual layer downwards.

Under C-type, the airflow exhibited shorter trajectories and slower movement. Notably, the trajectory profile (Fig. S8(c)-(d)) captures an extremely dramatic vertical intrusion, where a specific cluster (21.43%) plunged from the lower free troposphere (~700 hPa, >2000 m) down to the boundary layer. This intense vertical transport, coupled with high CWT values (~80 μg $m^{-3}$) over central/northern Henan (Fig. 9(b)), highlights the profound impact of deep vertical exchange driven by the cyclonic system.

Influenced by strong geostrophic winds under S-type, southwest airflow pathways dominated (Fig. 8(c)). The CWT analysis (Fig. 9(c)) identified a vast high-value source region (WCWT > 100 μg $m^{-3}$) encompassing the Central China urban agglomeration to the south, a vast region where intense anthropogenic $NO_x$ and VOCs emissions continuously fuel massive

daytime photochemical $O_3$ accumulation. The vertical profiles (Fig. S8(e)-(f)) confirm that a major portion of this southerly advection (~45.29%) subsided from the upper boundary layer (~880 hPa).

Finally, under WNE-type, the horizontal airflow was mainly concentrated on the northwest direction, accounting for 61.67% (Fig. 8(d)). The corresponding 3D altitude profiles (Fig. S8(g)-(h)) still capture a clear downward transport signal, revealing that this primary cluster originated from the upper residual layer (~800 hPa) 48 hours prior and subsided continuously. As these subsiding air masses passed over the potential source regions localized in central and northern Henan (CWT: 70-80 μg $m^{-3}$; Fig. 9(d)), they facilitated the downward entrainment and transport of $O_3$ to Xinxiang.

In summary, the 3D trajectory analysis demonstrates that the nocturnal $O_3$ spikes in Xinxiang are not merely driven by surface-level horizontal advection. Across all four weather types, the surface-arriving air masses systematically originated from the upper boundary layer or lower free troposphere, providing undeniable Lagrangian evidence of continuous downward $O_3$ transport from high-altitude reservoirs.

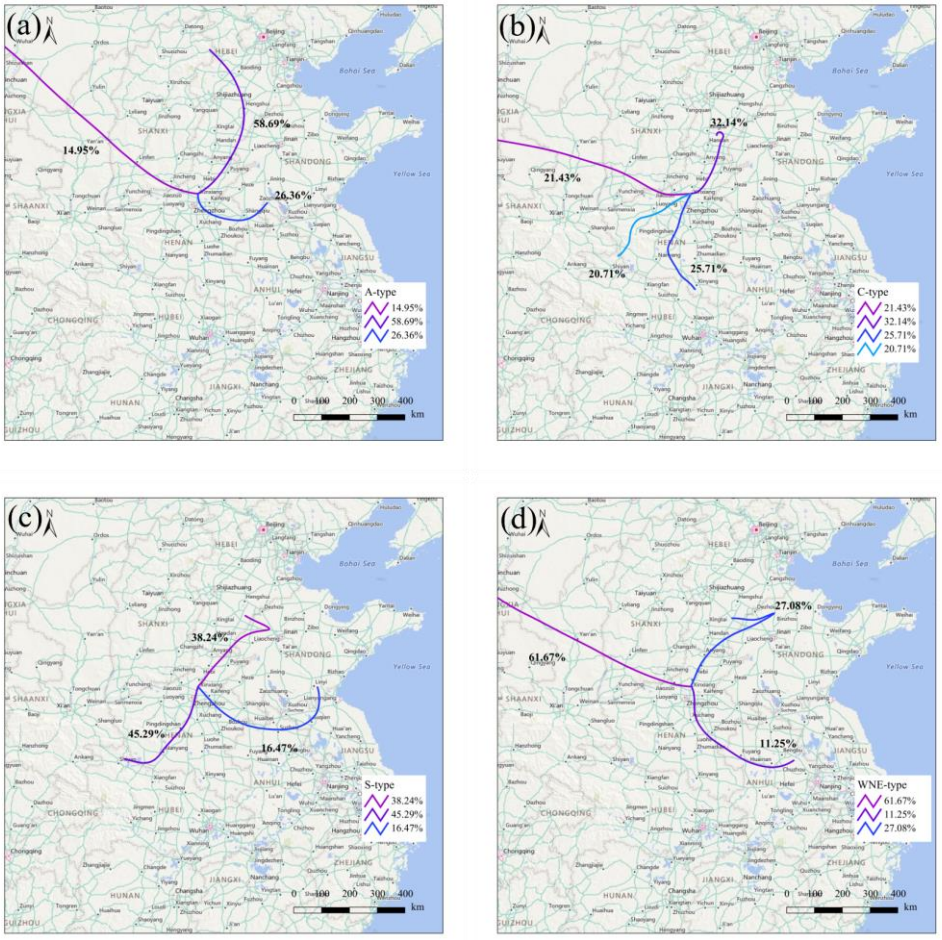
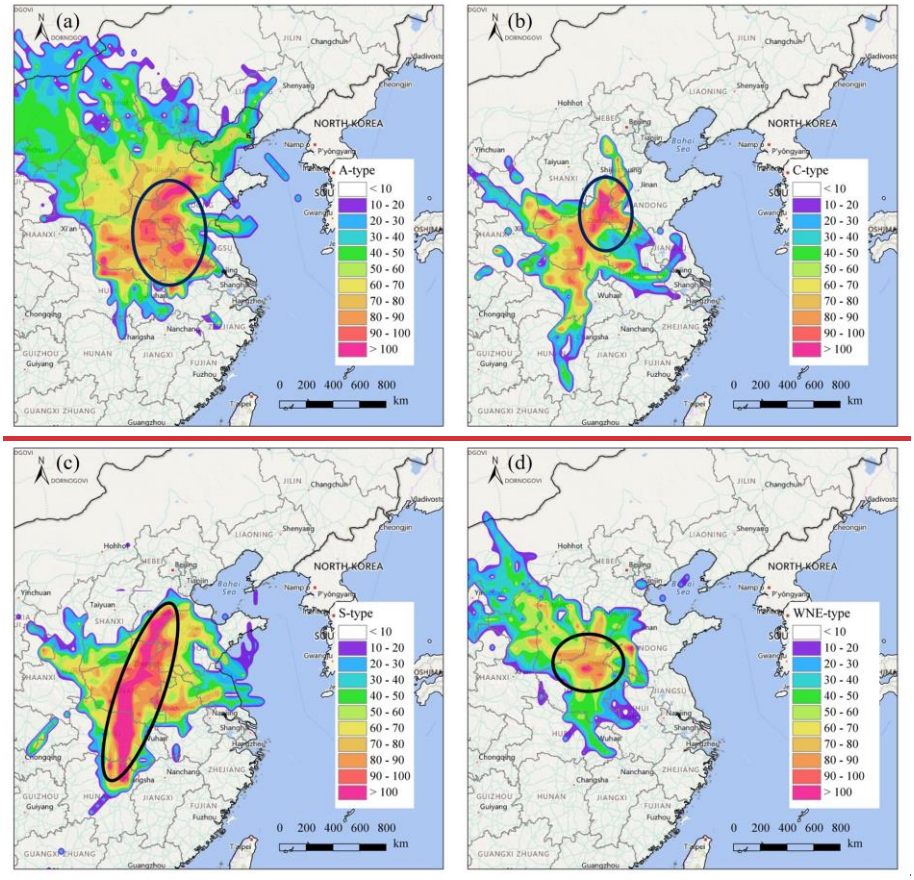



**Figure 8: Clustered backward trajectories under different weather types: (a) A-type, (b) C-type, (c) S-type, (d) WNE-type.**


(a)
A-type
(b)
C-type
(c)
S-type
(d)
WNE-type
< 10
10 - 20
20 - 30
30 - 40
40 - 50
50 - 60
60 - 70
70 - 80
80 - 90
90 - 100
> 100
0 200 400 600 800
km
NORTH KOREA

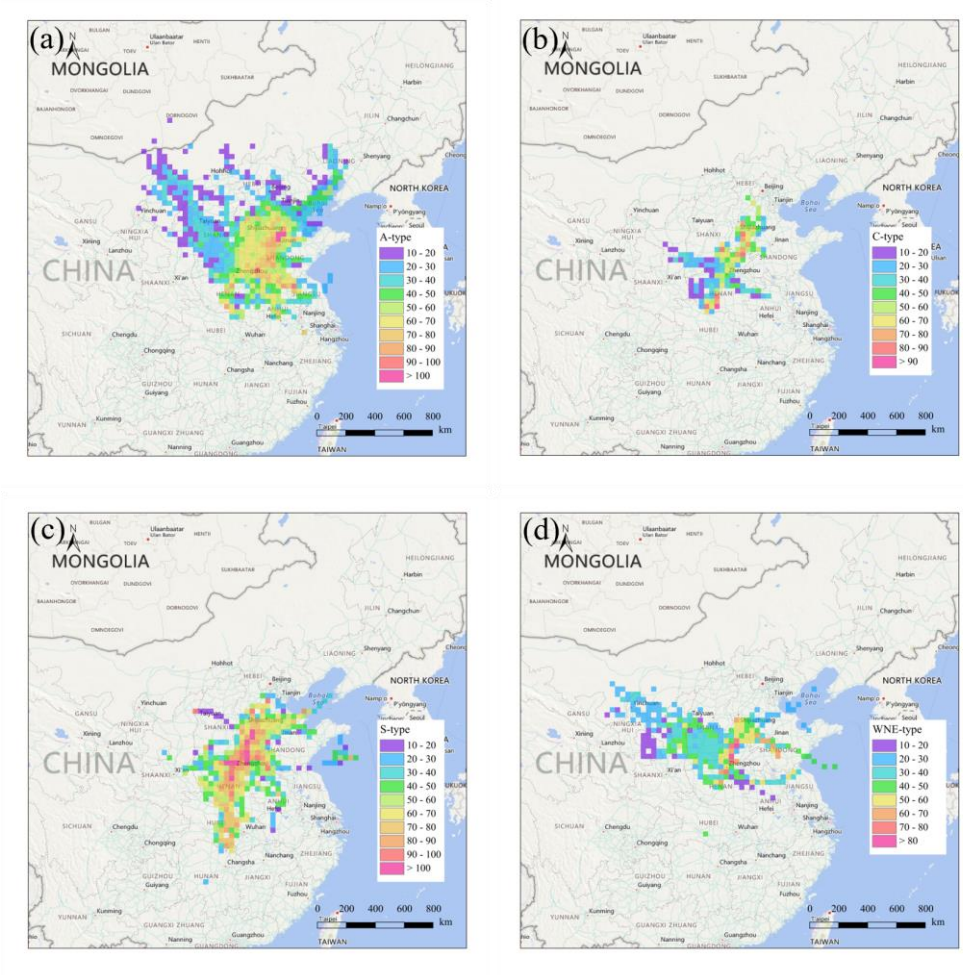



**Figure 49: Concentration weighted trajectory (CWT) analysis under different weather types: (a) A-type, (b) C-type, (c) S-type, (d) WNE-type ~~(black circles denote primary high-value areas of $O_3$)~~.**

~~In summary, the $O_3$ levels in Xinxiang under four weather types were all affected by regional transport, and mainly exhibited the characteristics of short distances and slow movement speeds.~~

### 3.4.2 ~~Vertical transport~~Vertical mixing and mechanical triggers

As established in Section 3.4.1, 3D trajectories confirm the synoptic delivery of air masses from high altitudes. However, to translate these high-altitude arrivals into surface NOI events, specific vertical transport mechanisms are required. To validate this process, we analyzed the vertical profiles of pressure velocity (Fig. 10), thermodynamic stability (Fig. S9), $O_3$ concentrations (Fig. S10), and surface turbulence metrics (Fig. 11).

The vertical $O_3$ profiles (Fig. S10) first confirm the fundamental prerequisite for NOI across all weather types: following sunset, a distinct nocturnal residual layer (RL) forms, clearly indicated by the high $O_3$ concentrations. Shielded from surface NO

titration and dry deposition, this RL successfully retains high daytime $O_3$, serving as the localized $O_3$ reservoir waiting to be tapped by downward forcing.

For A-type, the intrusion is primarily initiated by the systematic macroscopic subsidence of the continental high-pressure system. As explicitly shown in Fig. 10(a), a robust macro-scale downdraft dominates the vertical column over the Xinxiang region. This subsidence induces profound adiabatic compression, forming a significant low-level temperature inversion (1000-950 hPa) accompanied by low mid-level RH (Fig. S9). The inversion layer acts as a dynamic barrier, leading to marked vertical gradients in horizontal wind and sinking velocity and generating localized vertical wind shear. While the overall nocturnal surface environment remains highly stable and suppressed (consistent with the negative mean $\Delta U^*$ anomaly in Table S2), this localized shear interaction triggers intermittent, transient bursts of mechanical turbulence. These brief turbulent eddies, evidenced by the distinct nocturnal fluctuations in $U^*$ (Fig. 11), provide enough mechanical mixing to efficiently entrain the $O_3$-rich air from the residual layer down to the surface.

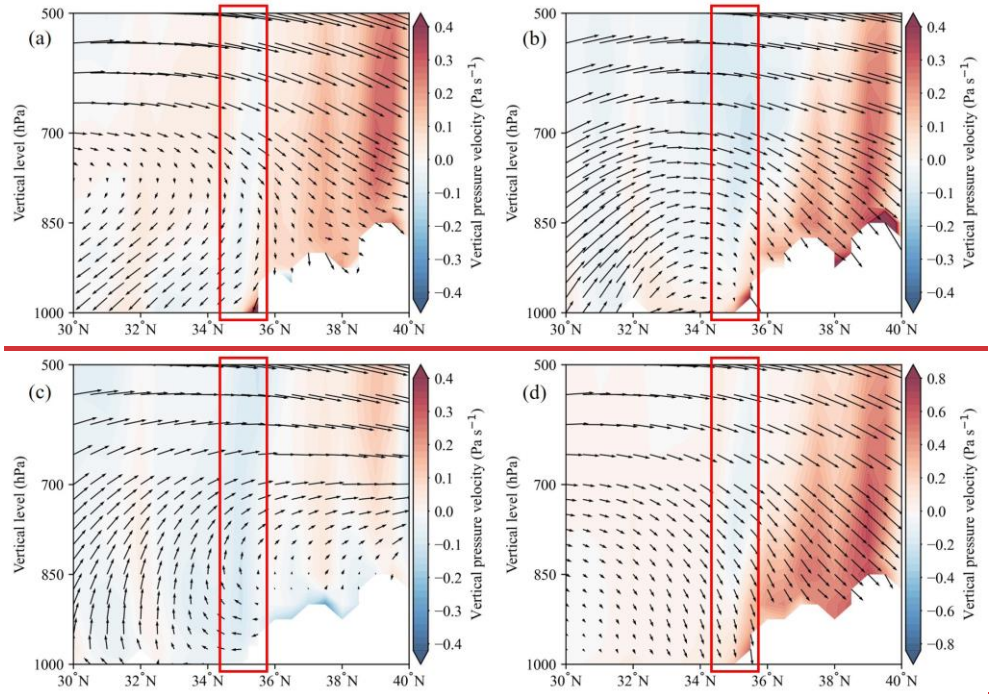
Under C-type, vertical mixing is dominated by localized mesoscale thermodynamics rather than uniform synoptic subsidence. As seen in Fig. 10(b), the vertical velocity field exhibits a complex coexistence of localized downdrafts and updrafts. The thermodynamic profiles (Fig. S9) corroborate this with a temperature inversion and mid-level dry air entrainment. This aligns perfectly with the cold pool mechanism: following convective rainfall, surface evaporative cooling generates a dense, subsiding pool of cold air. Simultaneously, the moderate CAPE values (86-314 J $kg^{-1}$) indicate residual thermodynamic instability driving localized shallow convection. The intense collision between these subsiding cold pools and localized convective motions creates severe turbulent mixing. This translates into the sharp nocturnal fluctuations in $U^*$ (Fig. 11), thereby increasing instability and dragging $O_3$-rich air from the RL into the surface.

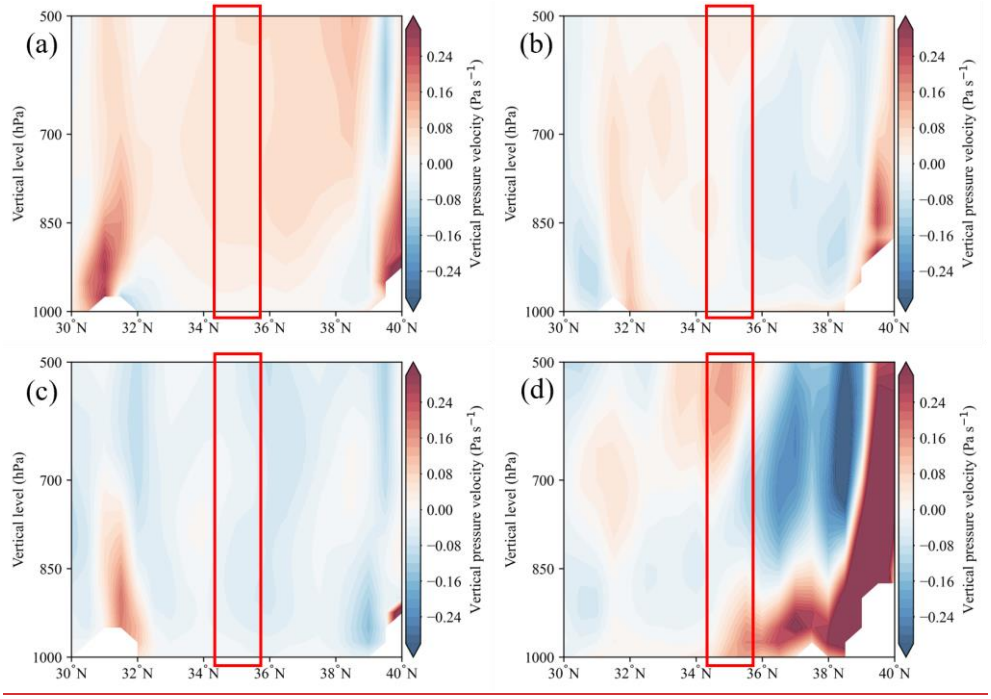
The local triggering mechanism under S-type relies fundamentally on intense mechanical shear overriding macro-scale lifting. S-type features strong southerly geostrophic winds. As this intense airflow approaches Xinxiang, it is forced upward by the Taihang Mountains, generating pronounced macro-scale orographic updrafts (Fig. 10(c)). However, to achieve the downward transport of $O_3$ against this macroscopic background lifting, a highly aggressive, localized boundary-layer mixing mechanism is essential. Specifically, the moderate CAPE values (257-295 J $kg^{-1}$) indicate persistent thermodynamic instability (Fig. S9), which fuels localized shallow convective motions within the nocturnal boundary layer. Simultaneously, anomalously strong near-surface horizontal winds (mean: $\Delta WS$ = 0.54 m $s^{-1}$; Table S2) forcefully interact with surface friction, inducing severe mechanical wind shear. The powerful synergy of this thermal instability and mechanical shear explicitly manifests as massive, sharp nocturnal spikes in $U^*$ and PBLH (Table S2 (mean: $\Delta PBLH$ = 102.41 m, $\Delta U^*$ = 0.06 m $s^{-1}$) and Fig. 11). Ultimately, this exceptionally enhanced turbulent mixing mechanically erodes the stable nocturnal inversion, overpowering the macroscopic updrafts to aggressively drag aloft $O_3$ from the residual layer down to the surface.

Finally, under WNE-type, downward transport is facilitated by an advection-driven mechanical shear mechanism. As explicitly shown in Fig. 10(d), the lower troposphere (below 850 hPa) is dominated by intense macro-scale subsidence. This induces a strong temperature inversion and extreme thermodynamic stability, corroborated by low CAPE values (22-23 J $kg^{-1}$) (Fig. S9), meaning thermal convective motions are completely suppressed. However, WNE-type is simultaneously driven by intense

horizontal advection. As this robust horizontal airflow passes over Xinxiang, intense near-surface vertical wind shear is produced. This macroscopic advective forcing translates directly into massive nocturnal spikes in boundary-layer turbulence, explicitly captured by $U^*$ and PBLH (Table S2 (mean: $\Delta$PBLH = 156.22 m, $\Delta U^*$ = 0.11 m $s^{-1}$) and Fig. 11). This enhanced nocturnal turbulence drives the downward transport of $O_3$ from the residual layer to the surface, thereby triggering the NOI events.

~~Fig. 5 illustrates the pressure vorticity and wind vectors in the vertical profile of Xinxiang. Under A-type, C-type, and WNE-type, there were strong downdrafts in Xinxiang (Fig. 5(a), (b) and (d)). For A-type and WNE-type, the occurrence of downdrafts was primarily associated with high pressure systems. Although C-type was controlled by a low-pressure system, Xinxiang would be affected by moist airflows during this period, accompanied by frequent heavy rainfall and active atmospheric convection. This easily led to the occurrence of local downdrafts. In contrast, under S-type, Xinxiang was located at the junction of the high-pressure and low-pressure systems. The pressure gradient force drove warm, moist air to rise along the frontal slope, resulting in updrafts (Fig.5(c)). Additionally, the Taihang Mountain to the north of Xinxiang acted as a topography barrier to southern geostrophic winds, enhancing low-level horizontal convergence and forcing vertical uplift of air.~~






**~~Figure 5: Vertical profiles of pressure vorticity and wind vectors under different weather types: (a) A-type, (b) C-type, (c) S-type, (d) WNE-type (red rectangles indicate the region of Xinxiang).~~Figure 10: Vertical profiles of pressure velocity under different weather types: (a) A-type, (b) C-type, (c) S-type, (d) WNE-type (red rectangles indicate the region of Xinxiang). In terms of vertical pressure velocity, negative values correspond to upward motion, while positive values indicate subsidence.**

~~Fig. S10 presents the vertical profiles of temperature and relative humidity in Xinxiang under four weather types. Under A-type, Xinxiang showed a significant low-level temperature inversion (with a temperature increase of 4.1–4.4 K from 975–950 hPa), which was attributed to the adiabatic compression induced by high-pressure subsidence, leading to the warming of lower-level air (Chen et al., 2022). For relative humidity profiles, we found that during 08:00 and 23:00 LT, mid-level (700–500 hPa) relative humidity remained below 50%, indicating that the subsiding airflow carried dry air (Chen et al., 2022). Although relative humidity displayed an increasing trend from 975 to 850 hPa, likely due to the mixing of subsiding airflow with locally evaporated moisture after reaching the ground (Feng et al., 2022), the pattern of dry air dominance in mid-level persisted. Additionally, CAPE values were extremely low at all times (ranging from 69 to 123 J kg$^{-1}$), reflecting stable atmospheric stratification with no significant convective potential. This aligned with high-pressure subsidence inhibiting upward motion. Under C-type, a significant temperature inversion layer (temperature increase of 7.6–9.1 K) existed in Xinxiang at 975–950 hPa for all time periods (2:00, 8:00 and 23:00 LT). This temperature inversion resulted from a cold-pool mechanism: after heavy rainfall, surface evaporative cooling produced a dense pool of cold air. As this cold pool spread outward, it forced the surrounding warm air to ascend while itself subsiding, thereby forming the inversion layer (Lochbihler et al., 2021). In terms of relative humidity, it was generally dry in mid-level (700–500 hPa), particularly at 02:00 (40.9–45.4%) and 08:00 LT (36.3–44.8%), reflecting entrainment of dry air by downdraft (Feng et al., 2022; Markowski and Richardson, 2011). This period was~~

~~frequently accompanied by rainfall, with relative humidity increasing at 975-850 hPa (e.g., from 45.5% to 54.2% at 02:00 LT), indicating precipitation evaporation and moist air accumulation in the cold pool. The vertical humidity structure suggested the coexistence of subsidence and convection. In addition, moderate CAPE values (148-265 J $kg^{-1}$) during this period indicated the presence of convective potential but limited intensity. This likely reflected: (1) Cold pool subsidence after heavy rainfall suppressed further convection, preventing the full release of CAPE (a process known as dissipating convection stage). (2) Local subsidence counteracted a portion of the ascending motion, thus restricting convective development (a process known as mesoscale subsidence suppression).~~

~~Under S-type, Xinxiang was situated in the transition zone between high and low pressure, and the frontal slope uplifted warm and moist air, facilitating the development of ascending motion. At 975-900 hPa, relative humidity was generally above 50%, especially at 23:00 LT (56.4-61.1%). This implied that moist air uplift released latent heat, enhancing convective instability (Feng et al., 2022; He and Chen, 2023). Moreover, southern geostrophic winds were blocked by the Taihang Mountain, which enhanced low-level horizontal convergence and forced air to ascend vertically. Moderate CAPE values (217-574 J $kg^{-1}$) also reflected a certain convective potential, and coupled with frontal lifting, it triggered shallow convection.~~

~~WNE-type and A-type had similarities in the vertical effects of high-pressure subsidence, which was mainly manifested in low-level temperature inversion and extremely low CAPE values (69-92 J $kg^{-1}$). Therefore, no further elaboration is needed here.~~

~~Figure S11 shows the vertical profiles of average $O_3$ concentration under four weather types. We found that high $O_3$ concentration was mainly distributed between 850 hPa and 1000 hPa, a range that lay primarily within the boundary layer during the daytime. After sunset, the nocturnal residual layer gradually formed, retaining part of the high $O_3$ concentration from the daytime. Surface $O_3$ continued to decrease due to processes such as NO titration and dry deposition, resulting in a significant $O_3$ concentration difference between surface and residual layer. Under A-type and WNE-type, influenced by the systematic subsidence of high-pressure systems, high $O_3$ concentration in the nocturnal residual layer was easily transported to the surface, leading to the occurrence of NOI events. Under C-type, vertical transport was predominantly driven by the cold pool mechanism, which generated localized subsidence, facilitating the downward transport of $O_3$ from the nocturnal residual layer to the surface. Under S-type, although upward airflow dominated in Xinxiang, vertical transport still occurred near surface, mainly related to shallow convection. The shallow convection acted as a dynamic driver, enabling the downward transport of $O_3$ from the nocturnal residual layer and inducing NOI events.~~

~~Figure S12 illustrates the diurnal variations of PBLH and $U^*$. It can be seen that under the four weather types, nocturnal PBLH or $U^*$ showed a fluctuating trend, with the most significant changes in $U^*$. This further indicated enhanced nocturnal~~

atmospheric instability, which in turn facilitated downward transport processes from the residual layer (He et al., 2022).

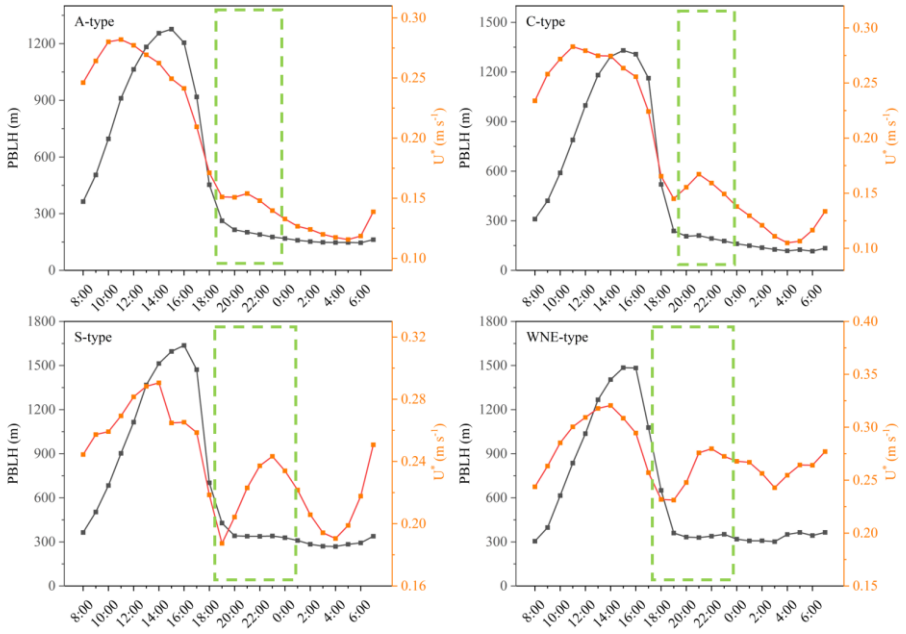



**Figure 11: Diurnal variations of planetary boundary layer height (PBLH) and friction velocity ($U^*$) in Xinxiang under four weather types (green dashed lines rectangles indicate the fluctuations of PBLH or $U^*$ during the night).**

## 4 Conclusions

This study systematically investigated the multi-scale synoptic drivers and underlying physical mechanisms governing NOI in a representative city on the North China Plain from 2021 to 2023. A high frequency of 392–470 NOI days was identified, with a distinct seasonal peak during the warm season (March–September). Approximately 71.35% of these events occurred between 00:00 and 06:00 local time, suggesting that the post-midnight period is highly susceptible to episodic perturbations of atmospheric stability, which facilitate the downward intrusion of $O_3$-rich air from the residual layer to the surface.

Subsequently, based on the Lamb–Jenkinson method, we categorized the synoptic backgrounds into four primary weather types: A type (57.36%), C type (11.17%), S type (20.81%), and WNE type (10.66%). Among them, A type exhibited the highest proportion, indicating that its meteorological conditions were most conducive to the formation of NOI days. Furthermore, A type mainly occurred in autumn; C type and S type frequently occurred in spring and summer; WNE type occurred with comparable frequency across all seasons.

The meteorological characteristics under different weather types varied significantly. A type was governed by high-pressure anticyclones, with a mild, dry, and moderately windy environment. In autumn, the mild weather conditions, stable atmospheric circulation, and the influence of the Siberian high collectively constituted the primary triggers for the high incidence of A type. C type was dominated by low-pressure systems and influenced by moist airflows, resulting in an increased risk of heavy rainfall locally. During C type, the higher average relative humidity (72.43%) and precipitation (0.49 mm $h^{-1}$) also

~~demonstrated heavy rainfall. In spring and summer, warm and humid meteorological conditions, active warm-moist airflows, enhanced atmospheric instability, and intensified convective activities collectively contributed to the high occurrence of C-type. S-type occurred within the transition zone between high and low pressure, influenced by southern geostrophic winds. In spring and summer, the high frequency of S-type was driven by the combined effects of the northward shift of the Western Pacific subtropical high, enhanced thermal vertical coupling, and the topography influence. WNE-type was controlled by high-pressure systems, affected by geostrophic winds with W-N-E direction. The unique geographical location, the alternating effects of multi-scale circulation systems, and topography influence together led to comparable occurrence frequency of WNE-type among all seasons.~~

~~Under four weather types, the formation of NOI days was influenced by regional transport, which was characterized by short distances and slow movement speeds, exacerbating local $O_3$ accumulation. Vertical transport of $O_3$ was driven by distinct triggers under different weather types. Under A-type and WNE-type, the vertical transport was mainly driven by the systematic subsidence of high pressure systems. C-type was primarily affected by cold pool subsidence airflow. S-type was mainly associated with shallow convection. These processes ultimately transported high $O_3$ concentration from the nocturnal residual layer to the surface, promoting the occurrence of NOI events.~~

~~Overall, our results demonstrate how synoptic-scale circulations modulate nocturnal boundary layer dynamics to trigger NOI. These findings offer an important physical perspective on the nocturnal $O_3$ budget and provide critical guidance for $O_3$ forecasting and pollution control in urban environments.~~

This study systematically investigated the synoptic drivers and underlying physical mechanisms governing NOI in a representative city in the North China Plain from 2021 to 2023. A high frequency of 370-444 NOI days was identified, with a distinct seasonal peak during the warm season (March-September). Approximately 69.53% of these events occurred between 00:00 and 06:00 local time, suggesting that the post-midnight period is highly susceptible to episodic perturbations of atmospheric stability, which facilitate the downward intrusion of $O_3$-rich air from the residual layer to the surface.

Subsequently, based on the Lamb-Jenkinson method, we categorized the synoptic backgrounds into four primary weather types: A-type (57.89%), S-type (19.88%), WNE-type (14.04%), and C-type (8.19%). Rather than simple seasonal dependencies, the occurrences and varying intensities of NOI were primarily determined by the distinct thermodynamic environments and evolutionary characteristics of these specific synoptic circulations. Specifically, A-type was characterized by a highly stable and suppressed local environment driven by anticyclones; C-type was dominated by low-pressure systems and moist advection, favouring atmospheric instability and convective activities; S-type was driven by a tight synoptic pressure gradient featuring strong southerly geostrophic advection, while WNE-type featured strong northwestern flows interacting with massive continental highs.

Under all four weather types, the development of NOI was significantly influenced by transport processes, which dictated the accumulation of upstream precursors and $O_3$. Furthermore, 3D regional trajectories provided Lagrangian evidence that the surface-arriving air masses systematically subsided from the upper residual layer or lower free troposphere (~880 to 700 hPa). Ultimately, translating these high-altitude arrivals into surface NOI events relied on distinct local mechanical triggers. Under

A-type, vertical transport was driven by systematic high-pressure subsidence; C-type was primarily triggered by severe mesoscale mixing from colliding cold-pool downdrafts and shallow convective motions; S-type was heavily dependent on a powerful synergy of localized convective instability and mechanical shear to overpower macro-scale orographic updrafts; WNE-type was facilitated by an advection-driven mechanical shear mechanism that overwhelmed the thermodynamic stability. Overall, our results demonstrate how synoptic-scale circulations cause NOI events. These findings offer an important physical perspective on the nocturnal $O_3$ budget and provide critical guidance for precise $O_3$ forecasting and dynamic pollution control in urban environments.

## Data Availability

The Global Data Assimilation System (GDAS1) dataset from the National Centers for Environmental Prediction (NCEP) is available at ftp:/arlftp.arlhq.noaa.gov/pub/archives/gdas1. The ERA5 reanalysis data can be accessed via https://www.ecmwf.int/en/forecasts/dataset/ecmwf-reanalysis-v5. The MERRA-2 data is obtained from https://gmao.gsfc.nasa.gov/gmao-products/merra-2.

## Author contribution

HW and LF designed the research. HW conducted data analysis and simulations, with all co-authors advancing the overall analysis further. HW wrote the paper with support from all co-authors.

## Competing interests

The contact author has declared that none of the authors has any competing interests.


## Financial support

This work was supported by the Demonstration research project on collaborative prevention and control of fine particulate matter and ozone pollution in Xinxiang (DQGG202133).


## References


Bell, B., Hersbach, H., Simmons, A., Berrisford, P., Dahlgren, P., Horányi, A., Muñoz-Sabater, J., Nicolas, J., Radu, R., Schepers, D., Soci, C., Villaume, S., Bidlot, J. R., Haimberger, L., Woollen, J., Buontempo, C., and Thépaut, J. N.: The ERA5 global reanalysis: Preliminary extension to 1950, Q. J. R. Meteorolog. Soc., 147, 4186-4227, https://doi.org/10.1002/qj.4174, 2021.

Chen, L., Chen, W., Hu, P., Chen, S., An, X., Ma, T., and Wang, Z.: Processes and mechanisms of the initial formation of the Siberian High during the autumn-to-winter transition, Clim. Dyn., 62, 315-329, https://doi.org/10.1007/s00382-023-06911-7, 2023.
Chen, T., Guo, J., Tong, B., Cohen, J. B., Chen, X., Yun, Y., Lv, M., Guo, X., and Lee, S. S.: Elucidating the impact of high- and low-pressure systems on temperature inversion from nine years of radiosonde observations in Beijing, Atmos. Res., 271, 106115, https://doi.org/10.1016/j.atmosres.2022.106115, 2022.
Chen, X., Huang, B., Li, M., Xiao, R., Cai, M., Zhou, Z., Ma, S., Gao, W., and Zhou, Z.: A prediction index of the volatile organic compounds pollution conditions in a chemical industrial park based on atmospheric stability, Sci. Total Environ., 919, 170862, https://doi.org/10.1016/j.scitotenv.2024.170862, 2024a.
Chen, Z., Liu, R., Wu, S., Xu, J., Wu, Y., and Qi, S.: Diurnal variation characteristics and meteorological causes of autumn ozone in the Pearl River Delta, China, Sci. Total Environ., 908, 168469, https://doi.org/10.1016/j.scitotenv.2023.168469, 2024b.
Cheng, J., Tong, S., Su, H., and Xu, Z.: Association between sub-daily exposure to ambient air pollution and risk of asthma exacerbations in Australian children, Environ. Res., 212, 113556, https://doi.org/10.1016/j.envres.2022.113556, 2022.
Cheng, X., Yu, J., Chen, L., Sun, Y., Zhang, H., Gao, S., Kong, S., Zheng, H., and Wang, H.: Influence of pollution control measures on the reduction of black carbon in an urban site of megacity, Tianjin, China based on ground-monitored and MERRA-2 reanalysis data, Sci. Total Environ., 912, 169466, https://doi.org/10.1016/j.scitotenv.2023.169466, 2024.
Chowdhury, F. I., Arteaga, C., Alam, M. S., Alam, I., and Resco de Dios, V.: Drivers of nocturnal stomatal conductance in C3 and C4 plants, Sci. Total Environ., 814, 151952, https://doi.org/10.1016/j.scitotenv.2021.151952, 2022.
Dong, Y., Li, J., Guo, J., Jiang, Z., Chu, Y., Chang, L., Yang, Y., and Liao, H.: The impact of synoptic patterns on summertime ozone pollution in the North China Plain, Sci. Total Environ., 735, 139559, https://doi.org/10.1016/j.scitotenv.2020.139559, 2020.
Duan, W., Chen, M., Huang, S., Dai, M., Wang, X., and Xu, L.: $PM_{2.5}$ prediction based on Lamb-Jenkinson method and LSTM neural network, Environ. Sci. & Technol., 43, 92-97, https://doi.org/10.19672/j.cnki.1003-6504.2020.01.014, 2020.
~~Eom, H. S. and Myoung Seok, S.: Seasonal and diurnal variations of stability indices and environmental parameters using NCEP FNL data over East Asia, Asia Pac. J. Atmos. Sci., 47, 181-192, https://doi.org/10.1007/s13143-011-0007-x, 2011.~~
~~Feng, X., Wang, S., and Guo, J.: Temperature inversions in the lower troposphere over the Sichuan Basin, China: Seasonal feature and relation with regional atmospheric circulations, Atmos. Res., 271, 106097, https://doi.org/10.1016/j.atmosres.2022.106097, 2022.~~
Gelaro, R., McCarty, W., Suárez, M. J., Todling, R., Molod, A., Takacs, L., Randles, C. A., Darmenov, A., Bosilovich, M. G., Reichle, R., Wargan, K., Coy, L., Cullather, R., Draper, C., Akella, S., Buchard, V., Conaty, A., da Silva, A. M., Gu, W., Kim, G.-K., Koster, R., Lucchesi, R., Merkova, D., Nielsen, J. E., Partyka, G., Pawson, S., Putman, W., Rienecker, M., Schubert, S. D., Sienkiewicz, M., and Zhao, B.: The modern-era retrospective analysis for research and applications, version 2 (MERRA-2), J. Clim., 30, 5419-5454, https://doi.org/10.1175/JCLI-D-16-0758.1, 2017.
Gilardi, L., Marconcini, M., Metz-Marconcini, A., Esch, T., and Erbertseder, T.: Long-term exposure and health risk assessment from air pollution: impact of regional scale mobility, Int. J. Health Geogr., 22, 11, https://doi.org/10.1186/s12942-023-00333-8, 2023.
He, C., Lu, X., Wang, H., Wang, H., Li, Y., He, G., He, Y., Wang, Y., Zhang, Y., Liu, Y., Fan, Q., and Fan, S.: The unexpected high frequency of nocturnal surface ozone enhancement events over China: characteristics and mechanisms, Atmos. Chem. Phys., 22, 15243-15261, https://doi.org/10.5194/acp-22-15243-2022, 2022.
~~He, W. and Chen, H.: More extreme heat occurrences related to humidity in China, Atmos. Oceanic Sci. Lett., 16, 100391, https://doi.org/10.1016/j.aosl.2023.100391, 2023.~~
He, Y., Wang, H., Wang, H., Xu, X., Li, Y., and Fan, S.: Meteorology and topographic influences on nocturnal ozone increase during the summertime over Shaoguan, China, Atmos. Environ., 256, 118459, https://doi.org/10.1016/j.atmosenv.2021.118459, 2021.
Hersbach, H., Bell, B., Berrisford, P., Hirahara, S., Horányi, A., Muñoz-Sabater, J., Nicolas, J., Peubey, C., Radu, R., Schepers, D., Simmons, A., Soci, C., Abdalla, S., Abellan, X., Balsamo, G., Bechtold, P., Biavati, G., Bidlot, J., Bonavita, M., De Chiara, G., Dahlgren, P., Dee, D., Diamantakis, M., Dragani, R., Flemming, J., Forbes, R., Fuentes, M., Geer, A., Haimberger, L., Healy, S., Hogan, R. J., Hólm, E., Janisková, M., Keeley, S., Laloyaux, P., Lopez, P., Lupu, C., Radnoti, G., de Rosnay, P.,

Rozum, I., Vamborg, F., Villaume, S., and Thépaut, J. N.: The ERA5 global reanalysis, Q. J. R. Meteorolog. Soc., 146, 1999-2049, https://doi.org/10.1002/qj.3803, 2020.
Holton, J. R. and Hakim, G. J.: An introduction to dynamic meteorology, Academic press2013.
Hoshika, Y., De Carlo, A., Baraldi, R., Neri, L., Carrari, E., Agathokleous, E., Zhang, L., Fares, S., and Paoletti, E.: Ozone-induced impairment of night-time stomatal closure in $O_3$-sensitive poplar clone is affected by nitrogen but not by phosphorus enrichment, Sci. Total Environ., 692, 713-722, https://doi.org/10.1016/j.scitotenv.2019.07.288, 2019.
Hu, C., Kang, P., Jaffe, D. A., Li, C., Zhang, X., Wu, K., and Zhou, M.: Understanding the impact of meteorology on ozone in 334 cities of China, Atmos. Environ., 248, 118221, https://doi.org/10.1016/j.atmosenv.2021.118221, 2021.
Ji, X., Hong, Y., Lin, Y., Xu, K., Chen, G., Liu, T., Xu, L., Li, M., Fan, X., Wang, H., Zhang, H., Chen, Y., Yang, C., Lin, Z., and Chen, J.: Impacts of synoptic patterns and meteorological factors on distribution trends of ozone in Southeast China during 2015–2020, J. Geophys. Res.: Atmos., 128, e2022JD037961, https://doi.org/10.1029/2022JD037961, 2023.
Li, J., Sun, Z., Lenschow, D. H., Zhou, M., Dou, Y., Cheng, Z., Wang, Y., and Li, Q.: A foehn induced haze front in Beijing: observations and implications, Atmos. Chem. Phys., 20, 15793-15809, https://doi.org/10.5194/acp-20-15793-2020, 2020a.
Li, K., Jacob, D. J., Shen, L., Lu, X., De Smedt, I., and Liao, H.: Increases in surface ozone pollution in China from 2013 to 2019: anthropogenic and meteorological influences, Atmos. Chem. Phys., 20, 11423-11433, https://doi.org/10.5194/acp-20-11423-2020, 2020b.
Li, L., Xie, F., Li, J., Gong, K., Xie, X., Qin, Y., Qin, M., and Hu, J.: Diagnostic analysis of regional ozone pollution in Yangtze River Delta, China: A case study in summer 2020, Sci. Total Environ., 812, 151511, https://doi.org/10.1016/j.scitotenv.2021.151511, 2022a.
Li, M., Zhang, Q., Zheng, B., Tong, D., Lei, Y., Liu, F., Hong, C., Kang, S., Yan, L., Zhang, Y., Bo, Y., Su, H., Cheng, Y., and He, K.: Persistent growth of anthropogenic non-methane volatile organic compound (NMVOC) emissions in China during 1990–2017: drivers, speciation and ozone formation potential, Atmos. Chem. Phys., 19, 8897-8913, https://doi.org/10.5194/acp-19-8897-2019, 2019.
Li, T., Wu, N., Chen, J., Chan, P.-w., Tang, J., and Wang, N.: Vertical exchange and cross-regional transport of lower-tropospheric ozone over Hong Kong, Atmos. Res., 292, 106877, https://doi.org/10.1016/j.atmosres.2023.106877, 2023.
Li, X.-B., Yuan, B., Wang, S., Wang, C., Lan, J., Liu, Z., Song, Y., He, X., Huangfu, Y., Pei, C., Cheng, P., Yang, S., Qi, J., Wu, C., Huang, S., You, Y., Chang, M., Zheng, H., Yang, W., Wang, X., and Shao, M.: Variations and sources of volatile organic compounds (VOCs) in urban region: insights from measurements on a tall tower, Atmos. Chem. Phys., 22, 10567-10587, https://doi.org/10.5194/acp-22-10567-2022, 2022b.
Li, Y., Liu, Y., Chen, Y., Chen, B., Zhang, X., Wang, W., Shu, Z., and Huo, Z.: Characteristics of Deep Convective Systems and Initiation during Warm Seasons over China and Its Vicinity, Remote Sens., 13, 4289, https://doi.org/10.3390/rs13214289, 2021.
Liang, D., Yan, H., Tian, Y., Liu, Y., Hao, S., Bai, H., Zhang, G., and Deng, W.: Identification of key controlling factors of ozone pollution in Jinan, northern China over 2013–2020, Front. Ecol. Evol., 10, 930569, https://doi.org/10.3389/fevo.2022.930569, 2022.
Liu, B., Wang, L., Zhang, L., Liao, Z., Wang, Y., Sun, Y., Xin, J., and Hu, B.: Analysis of severe ozone–related human health and weather influence over China in 2019 based on a high-resolution dataset, Environ. Sci. Pollut. Res. Int., 30, 111536-111551, https://doi.org/10.1007/s11356-023-30178-4, 2023.
Liu, J., Wang, L., Li, M., Liao, Z., Sun, Y., Song, T., Gao, W., Wang, Y., Li, Y., Ji, D., Hu, B., Kerminen, V.-M., Wang, Y., and Kulmala, M.: Quantifying the impact of synoptic circulation patterns on ozone variability in northern China from April to October 2013–2017, Atmos. Chem. Phys., 19, 14477-14492, https://doi.org/10.5194/acp-19-14477-2019, 2019.
Liu, N., He, G., Wang, H., He, C., Wang, H., Liu, C., Wang, Y., Wang, H., Li, L., Lu, X., and Fan, S.: Rising frequency of ozone-favorable synoptic weather patterns contributes to 2015–2022 ozone increase in Guangzhou, J. Environ. Sci., 148, 502-514, https://doi.org/10.1016/j.jes.2023.09.024, 2025.
Lochbihler, K., Lenderink, G., and Siebesma, A. P.: Cold Pool Dynamics Shape the Response of Extreme Rainfall Events to Climate Change, J. Adv. Model. Earth Syst., 13, e2020MS002306, https://doi.org/10.1029/2020MS002306, 2021.
Lu, X., Zhang, L., Chen, Y., Zhou, M., Zheng, B., Li, K., Liu, Y., Lin, J., Fu, T.-M., and Zhang, Q.: Exploring 2016–2017 surface ozone pollution over China: source contributions and meteorological influences, Atmos. Chem. Phys., 19, 8339-8361, https://doi.org/10.5194/acp-19-8339-2019, 2019.

Markowski, P. and Richardson, Y.: Mesoscale meteorology in midlatitudes, John Wiley & Sons, https://doi.org/10.1002/9780470682104, 2011.
Molod, A., Takacs, L., Suarez, M., and Bacmeister, J.: Development of the GEOS-5 atmospheric general circulation model: Evolution from MERRA to MERRA2, Geosci. Model Dev., 8, 1339-1356, https://doi.org/10.5194/gmd-8-1339-2015, 2015.
Monks, P. S., Granier, C., Fuzzi, S., Stohl, A., Williams, M. L., Akimoto, H., Amann, M., Baklanov, A., Baltensperger, U., Bey, I., Blake, N., Blake, R. S., Carslaw, K., Cooper, O. R., Dentener, F., Fowler, D., Fragkou, E., Frost, G. J., Generoso, S., Ginoux, P., Grewe, V., Guenther, A., Hansson, H. C., Henne, S., Hjorth, J., Hofzumahaus, A., Huntrieser, H., Isaksen, I. S. A., Jenkin, M. E., Kaiser, J., Kanakidou, M., Klimont, Z., Kulmala, M., Laj, P., Lawrence, M. G., Lee, J. D., Liousse, C., Maione, M., McFiggans, G., Metzger, A., Mieville, A., Moussiopoulos, N., Orlando, J. J., O'Dowd, C. D., Palmer, P. I., Parrish, D. D., Petzold, A., Platt, U., Pöschl, U., Prévôt, A. S. H., Reeves, C. E., Reimann, S., Rudich, Y., Sellegri, K., Steinbrecher, R., Simpson, D., ten Brink, H., Theloke, J., van der Werf, G. R., Vautard, R., Vestreng, V., Vlachokostas, C., and von Glasow, R.: Atmospheric composition change – global and regional air quality, Atmos. Environ., 43, 5268-5350, https://doi.org/10.1016/j.atmosenv.2009.08.021, 2009.
Nair, P. R., Chand, D., Lal, S., Modh, K. S., Naja, M., Parameswaran, K., Ravindran, S., and Venkataramani, S.: Temporal variations in surface ozone at Thumba (8.6°N, 77°E)-a tropical coastal site in India, Atmos. Environ., 36, 603-610, https://doi.org/10.1016/S1352-2310(01)00527-1, 2002.
Paoletti, E.: Ozone and Mediterranean ecology: plants, people, problems, Environ. Pollut., 157, 1397-1398, https://doi.org/10.1016/j.envpol.2009.03.001, 2009.
Sánchez, M. L., De Torre, B., García, M. A., and Pérez, I.: Ozone concentrations at a high altitude station in the Central Massif (Spain), Chemosphere, 60, 576-584, https://doi.org/10.1016/j.chemosphere.2004.12.079, 2005.
Shen, L., Diao, Y., Zhao, T., Gu, X., and Shi, S. S.: Meteorological influence on persistent $O_3$ pollution events in Wuxi in the Yangtze River Delta, China, Sci. Total Environ., 917, 170484, https://doi.org/10.1016/j.scitotenv.2024.170484, 2024.
Shi, J., Wu, X., Han, X., Zhong, Y., Wang, Z., and Ning, P.: Characterization and sources of carbonaceous aerosols in southwest plateau of China: Effects of biomass burning and low oxygen concentration, Atmos. Environ., 318, 120250, https://doi.org/10.1016/j.atmosenv.2023.120250, 2024.
Song, A., Yan, Y., Kong, S., Ma, J., and Tong, Z.: Impact of synoptic climate system interaction on surface ozone in China during 1950–2014, Atmos. Environ., 279, 119126, https://doi.org/10.1016/j.atmosenv.2022.119126, 2022.
Stein, A. F., Draxler, R. R., Rolph, G. D., Stunder, B. J., Cohen, M. D., and Ngan, F.: NOAA's HYSPLIT atmospheric transport and dispersion modeling system, Bull. Am. Meteorol. Soc., 96, 2059-2077, https://doi.org/10.1175/BAMS-D-14-00110.1, 2015.
Wang, D., Zhou, J., Han, L., Tian, W., Wang, C., Li, Y., and Chen, J.: Source apportionment of VOCs and ozone formation potential and transport in Chengdu, China, Atmos. Pollut. Res., 14, 101730, https://doi.org/10.1016/j.apr.2023.101730, 2023a.
Wang, G., Liu, X., Kong, F., Zhu, Z., Yan, P., Gao, W., and Zhao, N.: Characteristics of fine particulate matter in Linyi during the 24th Olympic winter Games: An insight into the components, sources, transport pathways, and source distribution, Atmos. Pollut. Res., 15, 102034, https://doi.org/10.1016/j.apr.2023.102034, 2024.
Wang, H., Fan, L., Deng, X., Huang, H., and Ye, D.: Research on the characteristics and triggering factors of concurrent events of ozone pollution and nocturnal ozone increase in Xinxiang, China, Atmos. Environ., 361, 121494, https://doi.org/10.1016/j.atmosenv.2025.121494, 2025.
Wang, H., Wang, H., Lu, X., Lu, K., Zhang, L., Tham, Y. J., Shi, Z., Aikin, K., Fan, S., Brown, S. S., and Zhang, Y.: Increased night-time oxidation over China despite widespread decrease across the globe, Nat. Geosci., 16, 217-223, https://doi.org/10.1038/s41561-022-01122-x, 2023b.
~~Wang, J., Chen, L., and Li, S.: Characteristics of spring Mongolian cyclones in the recent 70 years: Background circulations and weather influences, Int. J. Climatol., 44, 328-343, https://doi.org/10.1002/joc.8342, 2023c.~~
Wang, K., Xie, F., Sulaymon, I. D., Gong, K., Li, N., Li, J., and Hu, J.: Understanding the nocturnal ozone increase in Nanjing, China: Insights from observations and numerical simulations, Sci. Total Environ., 859, 160211, https://doi.org/10.1016/j.scitotenv.2022.160211, 2023d.
Wang, Y., Liu, R., and Xin, F.: Impact of atmospheric circulation patterns on ozone changes in the Pearl River Delta from 2015 to 2020, Environ. Sci., 44, 3080-3088, https://doi.org/10.13227/j.hjkx.202206106, 2023e.
Wu, J., Li, C., Ma, Z., Sun, Z., Zhu, X., and Dong, F.: Influence of meteorological conditions on ozone pollution at Shangdianzi station based on weather classification, Environ. Sci., 41, 4864-4873, https://doi.org/10.13227/j.hjkx.202003307, 2020.

Wu, Y., Chen, W., You, Y., Xie, Q., Jia, S., and Wang, X.: Quantitative impacts of vertical transport on the long-term trend of nocturnal ozone increase over the Pearl River Delta region during 2006–2019, Atmos. Chem. Phys., 23, 453-469, https://doi.org/10.5194/acp-23-453-2023, 2023.

~~Xia, R. and Zhang, D.-L.: An Observational Analysis of Three Extreme Rainfall Episodes of 19–20 July 2016 along the Taihang Mountains in North China, Mon. Weather Rev., 147, 4199-4220, https://doi.org/10.1175/mwr-d-18-0402.1, 2019.~~

~~Xu, H. and Yao, W.: A Numerical Study of the Beijing Extreme Rainfall of 21 July 2012 and the Impact of Topography, Adv. Meteorol., 2015, 980747, https://doi.org/10.1155/2015/980747, 2015.~~

Xu, J., Huang, X., Wang, N., Li, Y., and Ding, A.: Understanding ozone pollution in the Yangtze River Delta of eastern China from the perspective of diurnal cycles, Sci. Total Environ., 752, 141928, https://doi.org/10.1016/j.scitotenv.2020.141928, 2021.

Xue, Y., Wang, L., Jing, Y., Zhang, T., He, S., Ho, K. F., Huang, Y., Chen, L., Cui, L., and Cao, J.: Asian monsoon and local valley wind caused transport of volatile organic compounds episode across Qinling Mountain in China, J. Geophys. Res.: Atmos., 128, e2022JD038256, https://doi.org/10.1029/2022JD038256, 2023.

~~Yihui, D. and Chan, J. C. L.: The East Asian summer monsoon: an overview, Meteorol. Atmos. Phys., 89, 117-142, https://doi.org/10.1007/s00703-005-0125-z, 2005.~~

~~You, Y. and Ting, M.: Low Pressure Systems and Extreme Precipitation in Southeast and East Asian Monsoon Regions, J. Clim., 34, 1147-1162, https://doi.org/10.1175/jcli-d-20-0206.1, 2021.~~

You, Y., Wang, X., Wu, Y., Chen, W., Chen, B., and Chang, M.: Quantified the influence of different synoptic weather patterns on the transport and local production processes of $O_3$ events in Pearl River Delta, China, Sci. Total Environ., 912, 169066, https://doi.org/10.1016/j.scitotenv.2023.169066, 2024.

~~Zhang, Y., Sperber, K. R., and Boyle, J. S.: Climatology and interannual variation of the East Asian winter monsoon: Results from the 1979 95 NCEP/NCAR reanalysis, Mon. Weather Rev., 125, 2605-2619, https://doi.org/10.1175/1520-0493(1997)125<2605:CAIVOT>2.0.CO;2, 1997a.~~

Zhang, Y., Li, J., Li, J., Pan, X., Wang, W., Zhu, L., Wang, Z., Chen, X., Yang, W., and Wang, Z.: An intercomparison of ozone taken from the Copernicus atmosphere monitoring service and the second Modern-Era retrospective analysis for research and applications over China during 2018 and 2019, J. Environ. Sci., 114, 514-525, https://doi.org/10.1016/j.jes.2022.01.045, 2022.

~~Zhang, Y., Sperber, K., Boyle, J., Dix, M., Ferranti, L., Kitoh, A., Lau, K., Miyakoda, K., Randall, D., Takacs, L., and Wetherald, R.: East Asian winter monsoon: results from eight AMIP models, Clim. Dyn., 13, 797-820, https://doi.org/10.1007/s003820050198, 1997b.~~

Zhao, Y., An, X., Sun, Z., Li, Y., and Hou, Q.: Identification of health effects of complex air pollution in China, Int. J. Environ. Res. Public Health., 19, 12652, https://doi.org/10.3390/ijerph191912652, 2022.

Zhou, M., Zeng, Y., Li, J., Zhou, Y., Zhu, D., Luo, C., Zhuang, Y., Zhang, C., Wang, B., and Situ, S.: lmpact of atmospheric circulation patterns and volatile organic compounds on ozone pollution in Foshan City, Guangdong Province, Acta Sci. Circumst., 43, 215-225, https://doi.org/10.13671/j.hjkxxb.2023.0121, 2023.

Zhu, L., Han, X., Xu, L., Guan, X., Gong, A., Liu, H., and Zhang, M.: Nocturnal ozone enhancement in Shandong Province, China, in 2020–2022: Spatiotemporal distribution and formation mechanisms, Sci. Total Environ., 925, 171542, https://doi.org/10.1016/j.scitotenv.2024.171542, 2024.

Zhu, X., Ma, Z., Li, Z., Wu, J., Guo, H., Yin, X., Ma, X., and Qiao, L.: Impacts of meteorological conditions on nocturnal surface ozone enhancement during the summertime in Beijing, Atmos. Environ., 225, 117368, https://doi.org/10.1016/j.atmosenv.2020.117368, 2020.

Zhu, Y., Chen, D., Li, W., and Zhang, P.: Lamb-Jenkinson circulation type classification system and its application in China, J. Nanjing Inst. Meteor., 30, 289-297, https://doi.org/10.13878/j.cnki.dqkxxb.2007.03.001, 2007.